# ABSTRACT


| | |
|---|---|
| Title of Thesis: | REDUCTION OF MIXTURE PROPERTY VARIATION THROUGH CONTROL ON INITIAL MIXING DYNAMICS |
| | Marcelo Arispe-Guzman,<br>Master of Science, 2020 |
| Thesis Directed By: | Professor David I. Bigio,<br>Department of Mechanical Engineering |



Blend homogenization of a liquid-solid mixtures is achieved through mixer agitation which disperses the liquids and breaks up the agglomerates. Creating energetic or pharmaceutical blends requires a very low degree of mixture variation in the final product. Initial solid-liquid feeding protocols into the mixer greatly affect the ability to achieve low variation at minimal energy input. Experiments in a vertically oscillating mixer using dyed silicon oil and glass beads examined the effect of feed protocols, while varying acceleration and the number of cycles. A Central Composite Design (CCD) DOE revealed that the percent homogeneity and coefficient of variation measures of mixing are linearly dependent on acceleration and number of cycles. Experimental observations lead us to redefine the model for breakup of wet agglomerates. This study offers a starting point to developing feed protocols to improve the efficiency of oscillating mixers, such as the resonant acoustic mixer (RAM), for liquid-solid mixing.

# REDUCTION OF MIXTURE PROPERTY VARIATION THROUGH CONTROL ON INITIAL MIXING DYNAMICS

by

Marcelo Arispe-Guzman

Thesis submitted to the Faculty of the Graduate School of the
University of Maryland, College Park, in partial fulfillment
of the requirements for the degree of
Master of Science
2020

Advisory Committee:
Professor David I. Bigio, Chair
Professor Peter W. Chung
Professor Balakumar Balachandran
Assistant Professor Ryan D. Sochol

# Acknowledgements

Throughout the writing of this dissertation I have received a great deal of support and assistance.

I would first like to thank my advisor, Professor David I. Bigio, whose expertise was critical in formulating the research and methodology. Your guidance and feedback pushed me to sharpen my thinking and brought my work to a higher level.

I would like to acknowledge my lab associates at the Polymer Processing Lab for their collaboration. I would particularly like to thank Michael Flickinger for his assistance in conducting experiments and providing a different perspective of the research problem with his experience as a materials engineer.

I would also like to thank Manny Uy for his guidance in designing the experiment and determining the appropriate data analysis protocol within JMP software.

In addition, I would like to thank Ryan Smith and David Kreisberg for their machining experience. I could not have the mixing apparatus without their help.

Finally, I would like to thank my parents for their love and support. You are always there for me.

# Table of Contents

# List of Figures

# List of Abbreviations

| | |
|---|---|
| RAM | Resonant Acoustic Mixer |
| API | Active Pharmaceutical Ingredient |
| APAP | Acetaminophen |
| CCD | Central Composite Design |
| RSD | Relative Standard Deviation |
| DOE | Design of Experiment |
| MgO | Magnesium Oxide |
| DEM | Discrete Element Method |
| PDMS | Polydimethylsiloxane |
| HTPB | Hydroxyl Terminated Polybutene |
| IDP | Isodecyl Pelargonate |
| PBX | Polymer-Bonded Explosive |

# Chapter 1: Introduction

Mixing is critical to the production of pharmaceutical and energetic formulations. Creating homogeneous mixtures is essential to obtaining products with uniform content and performance. Blend homogeneity of solid-liquid systems is achieved by the dispersion of agglomerated solid particles and the distribution of fluid into the free volume around solid particles. Homogeneity is facilitated by the wicking of liquid into solid structures, increasing the importance of mixing dynamics to reduce length scales between ingredients and enable further wicking. The degree of homogeneity alters final mixture properties and becomes a crucial parameter for pharmaceutical and energetic industries [1]–[4]. Achieving homogeneity, however, becomes more difficult with the increase of solids volume fraction. Increasing the amount of active ingredients to enhance the potency of the product requires an understanding of the dynamics of creating homogeneous blends in highly-filled systems. Vertical oscillating mixers, such as the resonant acoustic mixer (RAM), are ideal apparatus for highly-filled systems. These types of mixers offer the benefit of increased mixing capability and reduction of mixture contaminants [5]–[7]. Zero-contact mixing pairs very well with degradable ingredients, such as those used by the pharmaceutical and energetic industries [8]–[10].

In this chapter, I will introduce the goal of powder mixing, whether it be dry or wet mixing, as to achieve the highest fill possible with a high degree of homogeneity. The methods in which high fill are achieved vary between dry and wet

systems. Mixing method and apparatus selection also affects the capability to achieve high-filled systems. Contact and contactless mixing methods are provided, each with their distinct advantages and disadvantages. The advent of the RAM and other vertically vibrating mixing methods are highlighted for their effectiveness in achieving homogeneity at reduced timescales.

## 1.1 Highly Filled Systems

In the field of polymer processing, the goal of mixing is to create uniform blends with reliable properties. Pharmaceutical formulations, for example, have strict quality regulations that need to be met before they can be introduced into the market [11]–[13]. Having formulations that perform below expectations can risk the safety of consumers and the reputation of the pharmaceutical company. Quality regulations are also common practice in the energetics industry. Polymer-bonded explosives (PBX) are compounds derived from polymer mixing processes. Undermixed PBX compounds carry the risk of premature detonation [14]–[16].

Mixing performance effectiveness varies depending on the scale of mixing. In industry it is not uncommon to want both reliability and potency. The potency of a blend is tied with its degree of fill pf the active ingredients. In the field of polymer processing, fill is characterized as the amount of the solid ingredient within the solid or liquid binding medium. Increasing the concentration of the active ingredient increases the effectiveness of the product but comes at the cost of larger mixing effort. Highly-filled systems pack materials into dense spaces and resist mixing forces due to frictional/surface interactions [17]. There is no shortness of mixing effort available to creating highly filled blend using ordinary mixing methods. However,

there is an advantage to creating highly filled systems with minimal mixing effort. These benefits come in the form of reduced operating costs and power requirements [18], [19].

### 1.1.1 Solids Mixing

Solids mixing refers to mixtures that are made entirely of solid particles. Highly-filled systems in solids mixing aim to minimize the void spaces between individual particles. These particles may be uniformly or irregularly shaped. In the case of uniformly spherical particles, the void space cannot be fully occupied by round solids due to geometry. Increasing the fill would mean filling the void spaces with smaller particles. Irregularly shaped particles can occupy more of the void space, but large void spaces are not easily filled as they are shape dependent. Particle size plays a significant factor in achieving highly filled systems. Mono-modal systems, those made up of a single sized particle, have a limit to the fill. The minimum free volume within a mono-modal system is 35% of the bulk volume and is achieved with a close packing structure. Polymodal systems have a greater chance of filling the void spaces left by the largest particles, and therefore are often used to make systems with high fill. Particle packing structures can also affect fill. Close packed structures are the limit to how close two particles can be and produce the smallest void spaces. This type of packing is only achievable through compression of the powder bed and is not always guaranteed. In practical applications, the packing can be reduced through compression of powder beds.

Solid mixing may also refer to breakup of agglomerates and dispersion within a solid medium. This is most common when using fine-sized particles. In smaller

diameters, gravitational effects become irrelevant and the surface area of the powder bed increases. The higher surface content, coupled with surface forces such as static, cause particles to stick together. The main function of the mixer is to reduce the agglomerates into the fine powder particles through physical interactions. The surface forces holding the agglomerate together are overcome by an external force, resulting in fracturing of the agglomerate. The breaking of clumps can be done gradually through erosion or abruptly through rupture [20], [21]. A more detailed look into the modes of breakup are presented in the next chapter.

### 1.1.2 Liquid-Solid Mixing

Liquid-solid refers to mixtures made of solid particles and liquid. It is common for the liquid to act as a binding agent, holding the solid particles together. Liquid-solid mixing is achieved through two processes. In the first process, solid particles are introduced into a stationary or flowing liquid medium. This can be, for example, introducing powder into a molten polymer medium through a twin-screw extruder. Solids, clumped or non-clumped, are fed into a liquid medium and are broken apart/dispersed by the shear rate of the fluid and by mixing elements within the mixer. The primary goal of this process is to disperse the solid particles throughout the liquid medium [22]. Doing so effectively increases the fill of the system and improves the properties of the mixture.

The second process is liquid flowing within the void space of a porous solid medium. This is a popular method in the energetics industry, where explosive particulate is bound together by a polymer binder. The solid particles can be stationary or moving. In either case, the liquid moves within the porous structure of

the solid, creating bridges that unify the solids together. In this process, the solids are the active ingredients and the goal of the mixing is to bind the solids together with the highest fill possible. As stated earlier, the void spaces can be occupied by smaller solids to increase fill. In liquid-solid systems this comes at the cost of less fluid to bind particles, resulting in brittle materials. Adding fluid will increase the bond strength of the binding agent but reduce overall fill. The challenge of this process is to distribute the liquid uniformly across the porous medium. Non-uniform regions often contain clumps of liquid and can cause swelling, further decreasing fill.

### 1.1.3 Demand for Powder Mixers

Highly filled mixtures are not naturally forming. Clumped particles and liquid bonded groups, for instance, are held together by surface forces and need externally supplied forces to overcome. Achieving homogeneity in a highly filled system also requires that ingredients are well distributed throughout the medium. Homogeneity is defined by the distribution of fluid within the solid and the dispersion of agglomerated solid particles. To produce homogenic mixtures, specially designed polymer mixers are used. These polymer mixers are suitable for different types of ingredients and each have their advantages. The function of the mixer is to provide the force necessary the break apart clumps and redistribute material. The required external forces are often a function of the ingredients involved; therefore, the mixers need to be controllable to produce the necessary mixing forces for the application. The effectiveness of powder mixers is an active area of research. Mixers can be split into two groups: Contact and Non-contact mixing.

## 1.2 Contact Mixing

Formulations requires external forces to break apart clumps and distribute material. These forces may be imposed by moving elements in the mixing apparatus. The elements make physical contact with the ingredients, inflicting stress to grouped particles be way of collisions or shearing of a flow field [20], [23]. Contact mixers include ribbon blenders and paddle mixers.

Ribbon blenders are well suited for solids mixing. They consist of a U-shaped trough and ribbon agitator. The ribbon agitator is comprised of a set of inner and outer helical members, held by a rotating central shaft. The outer and inner helixes move material in different directions. They are most commonly used in the food and pharmaceutical industries where bulk products are repeatedly blend [24]–[26]. Paddle mixers, on the other hand, can handle both solids and wet-dry systems. They utilize curved paddles radiating from the rotating central shaft to divide and blend material. Due to the angle of the paddles, these class of mixers exhibit good radial and axial mixing [27], [28].

### 1.2.1 Limitations

These types of mixers are limited by their wind-up time, mixing performance, and material choice. Making changes to the formulation is difficult because ingredients need to be purged from the mixing apparatus as to not chemically interfere with future blends. The ribbon and paddle mixers are notable for weak mixing performance near the central axis. These dead spots increase blend variation and are only circumvented with longer mixing durations. There is also an ample power requirement to mixing ingredients effectively, increasing cost of operation.

Since the mixing elements continuously make contact with the ingredients, there can be high local areas of stress that can degrade the material. In the case of energetic materials, it could case detonation; in the case of pharmaceuticals, it could cause degradation of the API potency.

### 1.3 Non-Contact Mixing

The external forces required for clumps to break apart and disperse can be achieved without the use of mixing elements. This can be achieved through rotation or vibration of the ingredients. Rotating contactless mixers, such as the tumbler blender, work best with dry materials. Diffusion is the main mechanism for mixing; batch materials cascade down and distribute particles over a freshly exposed surface as the vessel rotates along the horizontal axis. To accommodate the mixing flow, solids are generally loaded in layers rather than in bulk side-by-side. Tumble blenders operate at low impact and are appropriate for processing abrasive solids [23].

Vibrating contactless mixers, on the other hand, use the kinetic energy of particles from high frequency oscillations to create impact forces needed to break clumps. The resonant acoustic mixer (RAM) is the stand-out example of this mixing type. Created by the Resodyn Corporation, RAM vibrates ingredients at their natural resonance frequency, therefore reducing power requirements to sustain cyclic loading. It is able to achieve high oscillation by actively measuring the resonant frequency of the mixing vessel holding ingredients. It is then able to vibrate the stage the container rests on at the same frequency. The machine has control over the acceleration experienced by the materials. This is done by making small changes to the amplitude at the set resonant frequencies. Control over mixing time has led to the

development of mixing schedules for ingredients [5], [29]. Mixing schedules of acceleration and mixing time can be segmented together to increase performance and is an active area of research.

A significant advantage of the RAM is the inert environment of the mixing container. The container is made of glass and is chemically neutral. This allows for formulations that use hazardous or explosive materials to be safely handled without risk of contamination from mixing elements. This makes it very desirable to the energetics industry.

### 1.3.1 Limitations

Contactless mixers are limited by their finite volume output. This makes non-contact mixers unsuitable for mass production manufacturing of powder blends. This is remedied by increasing the size of the rotating or vibrating container but comes at the cost of added mass which translates to increased power requirement. In the case of the RAM, its main limitation is that there is a lack of research evaluating its performance [30]. It is a relatively new technology when it comes to powder mixing and there is still much not known about it, such as how the mixing schedules affect the mixing dynamics of ingredients. With very high acceleration output, it can be tempting to use the entirety of the RAM's mixing potential in each blend, but this can result in wasted power consumption and longer mixing times. A more efficient formulation is necessary, one that takes into account the breakup dynamics of the mixer.

# Chapter 2: Background

The creation of highly-filled systems is limited by the ability of the mixer to homogenize the ingredients. Achieving highly-filled systems using ordinary contact mixing methods has been possible for many decades thanks in part to the extensive work done evaluating and optimizing mixing performance [24], [25], [27], [31], [32]. Vertically vibrating non-contact mixing methods have only recently been developed, therefore understanding the performance of these class of mixers is an active area of research. In this chapter, I will present a literature review of vertically vibrating mixers. Through the literature review, I will demonstrate the mixing potential of vertically vibrated mixers, with a focus on resonant acoustic mixers. The dependence of mix homogeneity on mixing parameters of amplitude, frequency, and time will also be present for both dry and wet systems. The research conducted here will be useful in determining the modes of breakup of vertically vibrating mixers as well as providing the expected mixing behavior produced by amplitude, frequency, and time.

## 2.1 RAM Mixing Performance

Resonant acoustic mixing is a relatively new mixing technology developed by Resodyn Inc. Through vertical oscillations at high frequencies, the RAM is able to mix solid particulate in a fraction of the time it would take other traditional powder mixers. Although this is the case, the performance of RAM when mixing pharmaceutical formulations must first be evaluated before industry-wide utilization

is reached. The following studies on RAM mixing performance provide strong confirmation for using RAM in small-scale pharmaceutical applications.

### 2.1.1 Evaluation of Resonant Acoustic Mixing Performance

The effectiveness of RAM in pharmaceutical formulations has been evaluated by Muzzio and Osorio [5]. Their investigation into the mixing performance of RAM was split into two components. The first part was studying mixing performance as a function of active pharmaceutical ingredient (API) particle size, fill level, mixing intensity, and blending time using a fractional factorial design of experiments (DOE). The second part was a study on the mixing performance of API and lubricant as a function of acceleration, time, and fill level.

Their first experimental design illustrated the critical mixing parameters of the RAM. The variance used to indicate blend homogeneity was lowest for granulated APAP and higher for micronized APAP. The API type, differing in size and cohesiveness, led to significant variance differences ($p = 0.021$). API concentration ($p = 0.004$) and mixing acceleration ($p = 0.009$) were also found to significantly affect the blend homogeneity. Contrary to other closed contactless mixers, no significant differences on variance were obtained for differing fill levels ($p = 0.825$) or mixing time ($p = 0.829$). A mixing time of 1 minute was found to be sufficient in achieving blend homogeneity. The second experimental design examined the mixing curves as a function of time and acceleration. Overall APAP and lubricant homogeneity, as measured by relative standard deviation (RSD), was found to significantly decrease with increasing mixing time and acceleration ($p \leq 0.01$). At up to 1 minute of mixing, the acceleration had a significant effect on APAP and

lubricant homogeneity ($p = 0.01$). After 2 minutes, acceleration no longer has a significant effect on RSD ($p = 0.234$). Fill level did not yield statistically significant differences in blend homogeneity.

Muzzio and Osorio lay the groundwork for understanding powder mixing in a resonant acoustic mixer. Increasing mixing acceleration is correlated with improved blend homogeneity. Longer mixing times also improve performance but reach a peak with diminishing returns when mixing longer than 1 minute, or the critical mixing time. The significance on API type on mix quality suggests the critical mixing time is dependent on ingredient properties and likely the interaction between ingredients.

### 2.1.2 Verification of API Mixing Processes Using RAM Technology

Optimization of the RAM mixing process for active pharmaceutical ingredients has been conducted by Tanaka et al [7]. Optimization of RAM mixing parameters was done by numerical simulation. The simple harmonic oscillation of the RAM given by equation 2.1. Through differentiation of equation 2.1, the amplitude $A$, velocity $V$, and throw height $h$ were determined; where $x$ is distance, $\omega$ is angular frequency, $\alpha$ is phase lag.

$$x = A\cos(\omega t + \alpha) \tag{2.1}$$

$$x_{max} = \frac{\ddot{x}}{(2\pi f)^2} = A \tag{2.2}$$

$$V_{max} = \omega A = \frac{\ddot{x}}{2\pi f} \tag{2.3}$$

$$h = \frac{{V_{max}}^2}{2g} = \frac{\left(\frac{\ddot{x}}{2\pi f}\right)^2}{2g} \tag{2.4}$$

A simulation of RAM parameters was performed to determine appropriate acceleration and frequency conditions. Increased velocity and throw heights were shown to improve mixing efficiency as powder collisions were more frequent and over larger power. The optimum values of acceleration and frequency for RAM were 90-100 G and 60 Hz respectively. Powder mixing experiments carried out using various RAM conditions with a powder material of magnesium oxide (MgO) and lactose. A test on drug uniformity indicated that the optimal mixing conditions were 90-100 G and approximately 60 Hz, falling in line with the numerical optimization results. Compared to traditional mixing methods, showcased through testing on a V-shaped tumbler blender, the RAM was found to efficiently mix trace amounts of pharmaceutical powders. After mixing for only 0.03 hr on the RAM, the particles of the API were uniformly dispersed, whereas by ordinary methods 10 hr of mixing was necessary to achieve the same level of blend homogeneity. The superiority of RAM over ordinary mixing methods, and the ability to mix low drug content materials, make the RAM method applicable to pharmaceutical manufacturing processes.

## 2.2 Breakup Studies: Dry Systems

In a dry system clumped agglomerated bound together by surface forces, deagglomeration of the clumps is necessary to uniformly disperse ingredients. Dynamic analysis of particle breakup has been extensively studied for ordinary mixing methods including ribbon blenders, paddle mixers, and tumbler blenders [24],

[25], [27], [32]. With the advent of the RAM and other vertically vibrating mixers, understanding the transfer of energy from the vibrating plate to the powder will be vital in optimizing mixing parameters. The following studies dwell into the effectiveness of vertical vibrations in dry solids mixing as well as the convective flow fields that significantly improve dispersion is these types of mixing methods. The conclusions presented here will be instrumental to evaluating the mixing advantages of vertical vibrations in liquid-solid systems.

### 2.2.1 Particle Flow and Mixing in Vertically Vibrated Beds

The flow of solid particles in a vertically oscillating powder bed were studied by György Rátkai [33]. Particles inside a vertically vibrating cylindrical chamber flow in a sprout-like recirculating pattern. The internal friction of granular material is reduced to a great extent by the vibration. A low difference in height of thrown particles relative to the bed surface is sufficient in rolling particles from higher to lower levels. Rolled down particles are replaced when the vibration lifts the lowest layers of the powder column, thus creating the sprout-like recirculating flow field.

An experiment was conducted to determine the hydrodynamics of the particle flow, as functions of amplitude and frequency, on the vibro-sprouted system. The solid particles were two colored plastics of diameter 0.8–1 mm. The solids were layered across the chamber and the change in shape of the originally horizontal layers reveals the velocity profile of the granular bed. The diameter of the container was found to significantly effect particle flow in the bed. The power transferred from the vibrating plated spreads in the bed with a conical space. At large enough diameters, the cone-shaped vibratory effect will reach the walls and the recirculating flow field

will vanish. The vibro-sprouting flow can be advantageous for solids mixing due to the diffusive behavior of the flow. Experimentation with solids revealed an increase in mixing performance with increased amplitude and frequency, with 95% homogeneity being achieved in 12 minutes of mixing with an amplitude of 3.8 mm and frequency of 50 Hz. The degree of mixing was found to increase most rapidly during the first 3 minutes of mixing, followed by a gradual increase up to 95% homogeneity.

The study by György Rátkai highlights the advantage of vibration over other mixing methods, namely the fluidization of the powder bed to increase diffusion. The quality of the mixtures is also shown to be independently affected by amplitude and frequency but tends to increase when both amplitude and frequency increase. This suggests that the acceleration, which is a function of amplitude and frequency, plays a significant role in the homogenization of solids, and that it may be possible to optimize the mixing conditions to yield greater mixing performance at minimal mixing time.

### 2.2.2 Mixing in a Vibrated Granular Bed: Diffusive and Convective Effects

The mixing behavior of granulated particles in vibrated beds was investigated by Lu and Hsiau using discrete element method (DEM) simulations [17]. Convective displacements and diffusive motions are the two main factors influencing the mixing behavior of vibrating granular beds. An experiment using DEM was performed to determine the convective and diffusive motions. At a mixing frequency of 20 Hz, the velocity profile of the granulated particles exhibited a symmetric circulation pattern with an upward velocity at the center of the chamber and a downward velocity at the

walls. Convective and diffusive terms, $J_{conv}$ and $D_{yy}$ respectively, were recorded as functions of acceleration and frequency. These two terms are related by the Péclet number

$$Pe = \frac{J_{conv}\sqrt{gd^3}}{D_{yy}} \tag{2.5}$$

where $g$ is the gravitational acceleration constant and $d$ is the particle diameter. The Péclet number is found to increase first and then decrease with increasing acceleration, signifying the shift in convection and diffusion throughout the mixing process. This peak value occurs at a critical acceleration $\Gamma_{inf}$. As $\Gamma < \Gamma_{inf}$, $Pe$ increases with increasing $\Gamma$ and the symmetric convection flow has not yet been formed. As $\Gamma > \Gamma_{inf}$, $Pe$ decreases with increasing $\Gamma$ and the symmetric convection flow is now formed. With the symmetric convection flow in place, the rate of diffusive motion is increased.

The degree of mixing increases with vibration time, reaching a stationary value at longer time spans. For conditions where the symmetric convection flow is fully developed, the degree of mixing is found to be significantly higher than developing symmetric flows for the same time period. The work done by Lu and Hsiau illustrates the dependence of mixing homogeneity on the acceleration and frequency of vibration. The symmetric convection flow created in vertically vibrated powder beds is very advantageous to solids mixing, provided that the acceleration is above the specified threshold at the specified frequency.

## 2.3 Breakup Studies: Wet Systems

The cohesive forces binding particles together differs between dry and wet systems. In dry systems, the force is attributed to static forces that are present on the surfaces of particles [17]. In the case of wet systems, this cohesive force is a product of the liquid bridges formed between neighboring particles [34]. Thus, dispersion and distribution of particles in a wet-dry system requires breaking these liquid bonds. The hydrodynamic forces responsible for breakup have been widely investigated for wet-dry systems in shear flows [20], [21], [35]. Research on wet-dry mixing in vertically vibrated beds is scarce due to only recent advancements in vibrating mixing technologies. Nonetheless, early research on the topic demonstrates the ability to effectively mix wet-dry systems under vertical vibrations with careful selection of mixing parameters.

### 2.3.1 Hydrodynamic Analysis of the Mechanisms of Agglomerate Dispersion

The competition between hydrodynamic forces acting on an agglomerate and cohesive forces holding it together in dispersive mixing was studied by Manas et al [20]. From these competing forces, two modes of dispersion have been observed: cohesive and adhesive failure. Cohesive failure occurs when a fragment is broken off from an agglomerate, either un-infiltrated or infiltrated. This type of failure is responsible for dispersion by erosion or bulk rupture. Adhesive failure is characterized by a breakage at the interface between the infiltrated region and the dry boundary. Higher levels of infiltration tend to produce greater resistance to dispersion.

An experiment was conducted to provide insight into the modes of dispersion. In the experiment, fumed silica was infiltrated by polydimethylsiloxane (PDMS). Shearing the mixture revealed a dispersion behavior that did not follow classic erosion or rupture models. The dispersion behavior was a mix of both cohesive and adhesive failure. For dispersion to occur, the wetted region must be broken apart, meaning that the strength of both the wetted region and wet-dry interface provide resistance to dispersion[20], [36]. Under the assumption that the agglomerate is permeable, the hydrodynamic force, decomposed into tensile and shear forces, acting on the agglomerate can be written in spherical coordinates as

$$F_N = 5\pi\eta\dot{\gamma}R^2 \sin^2\Psi \sin^2\theta \sin\phi \cos\phi \tag{2.6}$$

$$F_S = \frac{5}{2}\pi\eta\dot{\gamma}R^2 \sin^2\Psi \sin\theta \sqrt{1 - \sin^2\theta \sin^2 2\phi} \tag{2.7}$$

where $\eta$ is the viscosity of the fluid, $R$ is the agglomerate radius, and $\dot{\gamma}$ is the instantaneous shear rate. Dispersion occurs whenever the mean stress, $\sigma_H$, exceeds the agglomerate stress at the interface, fracture surface $S_1$.

$$\sigma_H = \frac{F_H}{S_1} \tag{2.8}$$

This cohesive strength is assumed to be a constant in both un-infiltrated and infiltrated region, where the latter is higher in value to do the presence of liquid bridges. The stress holding the contents together is the capillary pressure (covered in more detail later). The capillary pressure is what holds the dry particles and the fluid together. For breakup and dispersive mixing to occur, the agglomerates present in the domain must be broken by a force grater then the force of the bonds keeping it

together. The shape of the region can also affect its tendency to break apart. Either erosion or rupture may happen depending on the fracture surface size. In the case where structural rearrangement is present, the agglomerate disperses by the adhesive failure mode.

### 2.3.2 DEM Study of Size Segregation of Wet Particles Under Vertical Vibration

A study on the segregation of wet particles through DEM simulations was done by Zhao et al [30]. Wet particle dynamics differ from dry particle dynamics. For instance, the static and dynamic characteristics of particles change when they are wet. Size induced segregation is also weakened by the cohesion force between wet particles. To simulate the segregation of wet particles, a linear cohesion model is used in the direct element method. The cohesion force, $F_{coh}$, is given by

$$F_{coh} = kA \tag{2.9}$$

where $A$ is the contact area and $k$ is the cohesion energy density, defined as the energy needed to remove a particle from its neighbors divided by the volume of the particle. Spherical and cubical particles are loaded into a cylindrical container in the DEM simulation environment. The spherical and cubical particles represent uniformly and nonuniformly shaped particles respectively.

The DEM simulations revealed that segregation behavior of wet particles is hindered by the cohesive force between particles when compared to simulation using dry particles. Segregation speed was significantly slower for cubical particles than with spherical particles. Investigations into the effect of cohesive force on the segregation revealed a hill-shaped segregation pattern where larger particles gather

near the container wall. Circulating flow was observed with spherical particle systems and were lacking in cubical systems. An increase in surface cohesion energy led to a decrease in overall segregation speed for the spherical particles but had little impact for cubical particles.

The segregation speed and final value of volume concentration of large particles, $C_L$, increased with an increase in mixing acceleration. Although this is the case, particle systems can be over-vibrated by excessive vibration acceleration (above 3.09 G), which is known as the critical acceleration value for a good performance of segregation [37]–[39]. Relatively low frequency and high amplitude is found to produce good segregation behavior for wet particle systems at a given vibration acceleration. This finding suggests that at the limit of vibration intensity defined by the acceleration, a proper combination of vibration parameters can significantly affect the homogeneity of the mixture.

## 2.4 Summary

Mixing in high shearing flows with dry particles has been extensively studied. Early work on the mixing effectiveness of vertically vibrating powder beds produced significant advantages of vibration mixing over traditional methods. The introduction of vertically vibrating mixers, such as the RAM, provide real benefits to the new mixing methods in industrial applications such as pharmaceutical formulations. Work on understanding the mixing behavior of vertically vibrating plates has only concerned dry systems thus far. Regardless, this work has shed important findings in the mixing performance of vertical vibrations.

The investigation done by György Rátkai reveals a relationship between the vibration amplitude, vibration frequency, and the rate of particle diffusion in a dry powder bed. This relationship is extended by the DEM simulations conducted by Lu and Hsiau. They attribute the increase in diffusion to the symmetric convection flow of solid particles. Amplitude and frequency, related by the acceleration of vibration, directly affect the development of the symmetric convection flow. There exists a threshold both amplitude and frequency must meet before the flow field is fully developed, at which diffusion of particles will be greatest. The rate of diffusion will continue to rise with increased amplitude and frequency, at which wasted performance become the primary concern. Muzzio and Osorio noted that long mixing times improve performance but reach a peak with diminishing returns when mixing longer than 1 minute. Even so, mixing below 1 minute was found to produce varying rates of diffusion heavily dependent on the amplitude and frequency of vibration.

Research on wet systems revealed the forces holding wet systems together, the capillary pressure. Manas et al present an in-depth overview of the modes of breakup in liquid-solid mixing: Erosion and Rupture. These two modes of agglomerate breakup occur at different scales and depend on the collision forces experienced by the wet clump. These two modes of breakup are expected to remain present in a vertically oscillating mixing environment.

The area that has not been studied exclusively is the initial mixing process. We will report on the effect of the feed protocol of the solids and the liquids and the operating parameters – Acceleration and number of cycles. The research conducted here will aid in determining the modes of adhesion of dry particles to the wetted

agglomerate and the modes of breakup in vertically vibrating mixers and gives a preview into the expected mixing behavior produced by amplitude, frequency, and time.

# Chapter 3: Liquid-Solid Mixing Dynamics

Liquid-solid systems are mixed through chemical and physical mechanisms. Chemical mechanisms refer to the surface interactions between the solid and liquid substances. Liquid naturally wants to penetrate the porous solid bed. Physical mechanisms refer to forced liquid dispersion. Mixing elements produce forces that aid in breaking up agglomerate and dispersing ingredients throughout the system. In this chapter I will cover the chemical mixing mechanisms of porous wicking and determine expression to determine wicking penetration based on the flow geometry. Physical mechanisms will be expressed through erosion and rupture. Finally, measures of mixing will be defined. These measures aim the define the degree of breakup as well as the degree of ingredient distribution.

## 3.1 Porous Wicking

The migration of liquid into porous media is partly facilitated by the capillary effect [40], [41]. Different surface energies between the both phases lead to the creation of a capillary pressure, leading to spontaneous suction of the wetting liquid into the porous material [42]–[44]. The capillary suction force is balanced by the viscous effects of the moving liquid front and leads to the Lucas-Washburn equation for modeling flow through porous media. The capillary pressure is also responsible for binding liquid and powder into agglomerates.

$$p_c = \frac{2\gamma cos(\theta)}{r_c} \tag{3.1}$$

### 3.1.1 Flow Through Semi-Permeable Solids

A porous medium is defined as a combination of interconnected voids permeable to flow. Using continuum approaches to solve for velocity distributions of resistance to fluid flow are only feasible through finite number of particles. In most practical applications of porous flow, the porous medium consists of millions of particles or fibers in irregular arrangements. Therefore porous-continuum approaches, which are the average of continuum models over the porous volume, have been developed to model flow in a porous medium [42].

The porous-continuum approach allows partial differential equations for pore-scale or microscopic mass, momentum, and energy balance to be transformed into macroscopic balance equations for flow in porous media [45]. In the can of a rigid porous network, the mass balance equation can be written as

$$\frac{\partial(\rho\varepsilon)}{\partial \mathrm{t}} \nabla \cdot \langle \rho \vec{v} \rangle = 0 \tag{3.2}$$

where $\langle \vec{v} \rangle$ is the pore-averaged fluid velocity, $\rho$ is density, and $\varepsilon$ is the porosity of the porous medium. Similarly, the momentum equation can be altered to a macroscopic form as

$$\langle \vec{v} \rangle = -\frac{K}{\mu} (\nabla \langle p \rangle - \rho \vec{g}) \tag{3.3}$$

where $\langle p \rangle$ is the pore-averaged pressure, $\mu$ is viscosity, $\vec{g}$ is gravitational acceleration, and $K$ is the permeability of the porous medium. The macroscopic form of the momentum equation is also referred to as Darcy's Law. This general equation models the fluid front velocity in either 1D, 2D or 3D flows.

### 3.1.2 Lucas-Washburn Porous Flow Approximations

The rate of fluid flow within porous materials in 1D flow is approximated by the Lucas-Washburn Model. The model determines the wicking depth of fluid inside a capillary tube. For application with porous media, the model assumes porous structure is a bundle of parallel capillary tubes [46]–[48]. The Lucas-Washburn model also assumes single-phase flow, complete saturation of fluid front, and isotropic permeability [42]. This model calculates the wicking depth as a function of material properties and time. The wicking distance of the liquid front $L$ is related to the surface tension $\gamma$, mean capillary radius $r$, wicking time $t$, contact angle $\theta$, and dynamic viscosity $\mu$.

$$L^2 = \frac{\gamma r t cos(\theta)}{\mu} \tag{3.4}$$

The Lucas-Washburn equation is derived from the balance between viscous and capillary forces in the porous medium and reduces to a balance of pressures in a constant diameter capillary tube. The pressure drop due to viscosity is found using the Hagen-Poiseuille law and can be reexpressed as

$$\Delta p = \frac{8\mu}{{r_c}^2} h\dot{h} \tag{3.5}$$

where $h$ is the height of a column wick or the penetration depth of a 1D flow in a porous material. The wicking distance can be solved through the balance of pressures using the boundary condition $h(t = 0) = 0$.

$$\frac{2\gamma cos(\theta)}{r_c} = \frac{8\mu}{{r_c}^2} h\dot{h} \tag{3.6}$$

$$\int_0^h h\, dh = \int_0^t \frac{r_c \gamma cos(\theta)}{4\mu}\, dt \tag{3.7}$$

$$h^2 = \frac{r_c \gamma cos(\theta)}{2\mu} t \tag{3.8}$$

### 3.1.3 Washburn Capillary Rise Experiment

The contact angle $\theta$ is unique to the liquid and solid material combination. It represents a fluid's capability of adhering to a material surface, with smaller contact angles indicating higher wetting tendency from the fluid [49]. The contact angle between the liquid and solid particles can be determined through the Washburn capillary rise experiment [50]–[52].

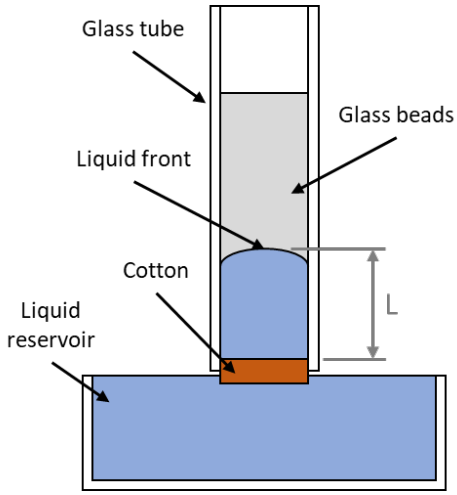


Figure 3.1: Washburn capillary rise experimental setup

In this experiment, powder is housed in a glass tube and suspended directly above a reservoir of fluid that rests on a mass scale. Separating the fluid and powder is a permeable film, in this case cotton. As liquid wicks through the film and powder, the mass of the penetrating liquid is recorded as a function of time. The contact angle

$\theta$ is then calculated in terms of previously mentioned material properties, fluid density $\rho$, porosity $\varepsilon$, and tube cross-sectional area $A$ [22].

$$m^2 = \frac{C\rho^2\gamma cos(\theta)}{\mu} \tag{3.9}$$

$$C = \frac{rA^2\varepsilon^2}{2} \tag{3.10}$$

### 3.1.4 Multi-Directional Porous Flow

Three-dimensional flow in a porous medium takes the form of source-like imbibition [53]. The direction of 3D flow is influenced by the permeability tensor $\boldsymbol{K}$. In swelling porous materials such as paper, for example, the liquid-absorbing fibers will swell differently in each principle direction depending on the orientation of the fibers. In non-swelling porous mediums, such as powder beds of irregular or uniform shape, the permeability is isotropic in each direction and thus the tensor is reduced to a scalar value. In the study we will be performing in the coming chapters, the working porous medium is a powder bed of irregularly and uniformly shaped particles. Thus, isotropic permeability applies, and flow will radiate equally in all directions from the point source. The permeability of the porous media is related to the particle diameter $d_m$ and porosity $\varepsilon$, and can be estimated using the Kozeny-Carman model:

$$K = \frac{{d_m}^2}{180}\frac{\varepsilon^3}{(1-\varepsilon)^2} \tag{3.11}$$

Source-like flow can be modelled using Darcy's Law. Assumptions made in the analysis are that the liquid front is spherical and that gravitational effects can be

neglected since hydrostatic pressure is much smaller than capillary pressure. Darcy's law reduces to

$$\langle \vec{v} \rangle = -\frac{K}{\mu} \nabla \langle p \rangle \tag{3.12}$$

The volumetric flow rate of the liquid at the front is

$$Q = 4\pi {r_f}^2 u_r \tag{3.13}$$

where $u_r$ is the radial velocity of the fluid front and $r_f$ is the distance from the source to the liquid front. The volumetric flow rate $Q$ can be expressed as a function of pressure gradient using Darcy's Law:

$$\frac{dp}{dr} = -\frac{\mu Q}{4\pi r^2 K} \tag{3.14}$$

The pressure at the source is $p_{atm}$ while the pressure at the liquid front is $p_{atm} - p_c$. In practical applications, the source would not be infinitesimally small. Fluid may be supplied by a tube, for example, and thus has a physical size $r_s$. Integrating equation 3.14 from the source to the front results in the capillary pressure

$$\int_{p_s}^{p_f} dp = -\frac{\mu Q}{4\pi K} \int_{r_s}^{r_f} \frac{dr}{r^2} \tag{3.15}$$

$$p_{atm} - p_c - p_{atm} = -\frac{\mu Q}{4\pi K} \left( -\frac{1}{r_f} + \frac{1}{r_s} \right) \tag{3.16}$$

$$p_c = \frac{\mu Q}{4\pi K} \left( \frac{1}{r_s} - \frac{1}{r_f} \right) \tag{3.17}$$

Combining equations 3.13 and 3.17, along with $u_r = \frac{dr_f}{dt}$, yields

$$\frac{Kp_c}{\mu} = {r_f}^2 \frac{dr_f}{dt}\left(\frac{1}{r_s} - \frac{1}{r_f}\right) \tag{3.18}$$

and can be integrated, with $r_f = r_s$ as the initial condition, to express time-dependent liquid front as

$$\frac{1}{3r_s}\left({r_f}^3 - {r_s}^3\right) - \frac{1}{2}\left({r_f}^2 - {r_s}^2\right) = \frac{Kp_c}{\mu}t \tag{3.19}$$

In cases where fluid is finite in volume, equation 3.19 is only valid until the source fluid has depleted. Given a total fluid volume $V_{fl}$ and assuming fluid leaves the source region of radius $r_s$, the fluid front radius $r_f$ can be calculated as:

$$r_f = \sqrt[3]{\frac{3V_{fl}}{4\pi\varepsilon} + {r_s}^3} \tag{3.20}$$

## 3.2 Erosion and Rupture

The mixing of liquid and solid particles can be facilitated by breaking apart wet agglomerates through agitation. The wet agglomerates are held together by the capillary pressure and are broken apart by two physical mechanisms: erosion and rupture [20]. Erosion is the removal of small fragments from the wet agglomerate. The capillary pressure bonding the surface of these small fragments is easily overcome by the mixing forces and is the dominant breakup mechanism when small hydrodynamic forces are present. Increasing hydrodynamic forces introduces rupture to the dispersion mechanism. Rupture represents abrupt breakage of the wet agglomerate into large aggregates. Through these two mechanisms, liquid is effectively dispersed throughout the media.

The dispersive mechanisms of erosion and rupture are made possible by the hydrodynamic force and duration. In vibration-based mixers, hydrodynamic force is often represented by acceleration a as used in the literature [5]. The duration of acceleration is often expressed as time $t$, but this measure assumes that the hydrodynamic forces produced by the acceleration are present throughout the entire mixing duration. The hydrodynamic forces acting on the wet agglomerate are only present once per mixing cycle, when free falling ingredients collide with the container after being thrown upwards [7]. Collisions occurs periodically, therefore the best measure for mixing duration is the number of cycles $N$.

## 3.3 Measures of Mixing

A value or scale for mixing is necessary to determine the quality of a mixture. must be present to determine whether a mixture is mixed well. Mixing measures can take a variety of approaches. The quality of a mixture can be measured through destructive testing, for instance. In the energetics industry, PBX mixtures are tested for uniformity through burning performance of the explosive compound. In a lab environment, active ingredients are often substituted with ingredients of similar shape and size to reduce consumption cost and reduce potential health risks to researchers. This is especially true for energetic material which will ignite if handles improperly. In these scenarios, field experiments to determine mixedness are not possible and therefore a different measure of the mixing quality must be made. Without field testing, the quality of mixtures can be quantified using optical means. In a mixture of two ingredients, blend homogeneity is achieved when neither ingredient is individually recognizable [54], [55]. In other words, mixing is complete when the

local concentration of each ingredient matches the global concentration of each ingredient. This is often observed through differences in color throughout the mixed medium. Mixing measures are obtained by quantifying the dispersion and distribution of ingredients.

### 3.3.1 Scale and Intensity of Segregation

Danckwerts defined the measure of "goodness of mixing" as (a) being closely related to the properties of the mixture, (b) able to make measurements conveniently, (c) applicable to as many different types of mixtures as possible without modification, and (d) should not depend on arbitrary tests without physical significance [56], [57]. In a powder mixing process, clumped ingredients are continually broken down in size and distributed throughout the system. According to Danckwertz, the quality of a mixture is defined by two principles: how much clumps have broken down and how well they have been distributed. These two principles are called the scale of segregation and the intensity of segregation.

The scale of segregation defines the extent to which ingredients have broken down. For a well-mixed blend, the concentration of each ingredient $A$ and $B$ is equal to the mean concentration of those ingredients even at the smallest length scales. The expression

$$R(r) = \frac{\overline{(a_1 - \bar{a})(a_2 - \bar{a})}}{\overline{(a - \bar{a})^2}} = \frac{\overline{(b_1 - \bar{b})(b_2 - \bar{b})}}{\overline{(b - b)^2}} \tag{3.21}$$

defines the coefficient of correlation between volume concentrations $a$ and $b$, separated by a distance $r$. At small length scales, $R(r)$ is generally close to 1 because points close together are likely to be of the same clump. At larger length scales, $R(r)$

will fall to 0 as the relationship between those two concentrations is undefined or random. The scale of segregation can be found through either a linear scale $S$ or a volume scale $V$

$$S = \int_0^{\xi} R(r)dr \tag{3.22}$$

$$V = 2\pi \int_0^{\xi} r^2 R(r)dr \tag{3.23}$$

where $\xi$ is the value of $r$ for which $R(r)$ falls to zero. Scales $S$ and $V$ represent the areas under the curves $R(r)$ and $r^2R(r)$ respectively. By this definition, the scale of segregation is greatest when $\xi$ is its largest.

The intensity of segregation, $I$, represents the extent to which the concentrations $A$ and $B$ in the clumps depart from the mean concentrations regardless of clump size. This mixing measure is defined as

$$I = \frac{{\sigma_a}^2}{\bar{a}(1-\bar{a})} = \frac{{\sigma_b}^2}{\bar{b}(1-b)} \tag{3.24}$$

where ${\sigma_a}^2$ and ${\sigma_b}^2$ are the variances of $a$ and $b$ respectively. By this definition $I$ has a value of 1 when segregation is complete (ingredients $A$ and $B$ are completely separated from each other) and 0 when concentration is uniform.

### 3.3.2 Shannon Entropy

A perfect mixture is achieved when the local concentration of ingredients in any region of the mixture is the same as the global concentration [58]. The quality of mixtures is limited by the scale of observation, however. Mixtures may appear

uniform at a distance, but upon closer inspection each ingredient becomes distinct. Therefore, mixing must be quantified as a function of scale of observation. Shannon entropy is used to measure disorder and lack of information and can be adapted to polymer processing to measure mixing quality based on the randomness of the mixture. To adapt Shannon entropy to polymer processing, a system of $C$ different species is divided into $M$ bins. The probability a particle of species $c$ is in bin $j$ is given by

$$p_{j,c} = \frac{\frac{n_{j,c}}{P_c}}{\sum_{i=1}^{M}\sum_{c=1}^{C}\frac{n_{i,c}}{P_c}} \tag{3.25}$$

where $n_{j,c}$ is the number of particles of species $c$ and $P_c$ is the overall system population. These joint probabilities can be used to calculate the Shannon entropy of the system:

$$S = -\sum_{j=1}^{M}\sum_{c=1}^{C} p_{j,c} \ln p_{j,c} \tag{3.26}$$

Shannon entropy operates in a 0-1 scale and is maximized when all $P_{j,c}$ are equal. In other words, at each location $j$, the concentration of each component is the same as the whole system. Entropy is additive and can be divided into two other entropies: the conditional entropy $S_{location}(species)$ and the entropy of spatial distribution $S(location)$. The latter is associated with the spatial homogeneity of particles regardless of their species. The former quantifies the mixing of the species and is location specific. The expressions for entropy are defined here

$$S = S_{location}(species) + S(location) \tag{3.27}$$

$$S_{location}(species) = \sum_{j=1}^{M} p_j S_j(species) \tag{3.28}$$

$$p_{\frac{c}{j}} = \frac{\frac{n_{j,c}}{P_c}}{\sum_{c=1}^{C} \frac{n_{j,c}}{P_c}} \tag{3.29}$$

$$p_j = \frac{\sum_{c=1}^{C} \frac{n_{j,c}}{P_c}}{\sum_{i=1}^{M} \sum_{c=1}^{C} \frac{n_{i,c}}{P_c}} \tag{3.30}$$

$$S_j(species) = -\sum_{c=1}^{C} p_{\frac{c}{j}} \ln p_{\frac{c}{j}} \tag{3.31}$$

$$S(location) = -\sum_{j=1}^{M} p_j \ln p_j \tag{3.32}$$

where $p_j$ is the probability that a group of particles is in bin $j$ regardless of species makeup and $p_{\frac{c}{j}}$ is the conditional probability to find $P_c$ particles of species $c$ in bin $j$.

### 3.3.3 Percent Homogeneity and Coefficient of Variation

Completely uniform mixtures are not practically achievable. Instead, the limit in uniformity a mixture can obtain is a completely randomized mixture in which the probability of finding a particle of any component is the same at all locations [59]. A randomized mixture defines the limit of mixing possible and is used in the Poole mixing index, $M_{Poole}$, as a measure to mixing quality

$$M_{Poole} = \frac{\sigma}{\sigma_r} \tag{3.33}$$

where $\sigma$ is the observed standard deviation of the mixture and $\sigma_r$ is the standard deviation of a completely random mixture. A random mixture is not always easily achievable and is adapted to image processing means where randomized mixtures can be artificially created.

The Poole mixing index $M_P$ of the respective sample images is determined by dividing images into non-overlapping macro-pixels, each of which containing a mean $\bar{X}_i$ and standard deviation $Sd_i$. The average of macro-pixel standard deviations $\bar{M}_{Sd}$ is computed and compared with the same measure for a randomized version of the image. The randomized image represents a fully homogenized blend and is obtained by randomizing the pixel locations of the sample image [59]. The percent homogeneity, $H\%$, is obtained as follows:

$$\bar{M}_{Sd} = \frac{1}{N}\sum_{i=1}^{N} Sd_i \tag{3.34}$$

$$M_{Poole} = \frac{\bar{M}_{Sd}}{\bar{M}_{Sd_{random}}} \tag{3.35}$$

$$H\% = M_{Poole} \times 100\% \tag{3.36}$$

Final product variation is also an important factor as high variation leads to inconsistent product behavior. Reducing the variation ensures that all regions of the batch behave equally, improving product precision and repeatability. This measure approaches 0 in uniform mixtures and can be normalized to compare the quality of

different mixtures. Normalized variation, expressed as the coefficient of variation, is also useful in image processing applications. Subtle differences in ambient lighting affects the grayscale color mapping of the final product and is mitigated through a normalization of variation. The coefficient of variation, $C_v$, is the standard deviation of the micropixel means normalized by the mean value of the entire image.

$$\sigma_m = \sqrt{\frac{1}{N}\sum_{i=1}^{N}(\bar{X}_i - M_t)^2} \tag{3.37}$$

$$C_v = \frac{\sigma_m}{M_t} \tag{3.38}$$

# Chapter 4: Experimental Materials

The performance of a mixing process can vary heavily with the material properties of the ingredients [7]. In wet-dry systems, the liquid selection affects mixing dynamics through its surface tension and viscosity material properties. For example, the wicking depth modeled by the Lucas-Washburn equation is decreased as the viscosity of the fluid increases. The solid powder selection can also affect wicking with its particle size, porosity, and surface texture. The contact angle introduced in chapter 3 affects the fluid's ability to adhere to the solid and is affected by the solid surface texture. Particle size and porosity affect the void space within the porous medium, altering the capillary pressure that draws in fluid. In this chapter, I will introduce the ingredients used in the static and dynamic experiments covered in chapters 5 and 6 respectively. Reasoning behind the material selection and the process for obtaining material properties will also be detailed.

## 4.1 Solid Selection

Glass beads and granulated sugar of diameter 100 and 300 μm were used as the working powders to carry out the experiments. Glass beads are uniformly round, giving them isotropic material properties [60]. As such, glass beads remove uncertainty in void geometry and surface interactions with liquid. This enables the cohesive failure of liquid bridges to be simplified and generalized. Granulated sugar particles, in contrast to glass beads, are non-uniformly shaped and have surface roughness which increases friction between particles and helps dissipate mixing

forces [61]. Although there is uncertainty in its behavior, its morphology makes it a good substitute for pharmaceutical compounds and explosive particulate [3].

The two sizes of powder, 100 and 300 μm in diameter, are within the size of powder used in both pharmaceutical and energetic industries [31]. In the case of the glass beads, a combination of 100 and 300 μm particles were considered. The different concentrations of each size the void space, and therefore mean capillary radius, changes and results in different wicking/wetting behavior. In industry, mixtures of two particle sizes (bimodal) are used to increase the fill of active ingredients, resulting in more chemically potent mixtures.

### 4.1.1 Sieving Process

Glass beads were purchased from Kramer Industries Inc. and ranged in size from 50-70 mesh for the larger sized particles targeting 300 μm and 100-170 mesh for the smaller sized particles targeting 100 μm. Granulated sugar was sourced from Domino Sugar in coarse and fine variants targeting particles sizes of 300 and a00 μm respectively. The particles were sieved using 58/61 mesh screens for 300 μm particles and 140/206 mesh screens for the 100 μm particles.

Particles in each size category were hand-sieved using the coarse mesh screen. Particles unable to pass through the sieve were grinded in a blender to reduce their size and sieved once again. The process was continued until all the powder passed through the coarse sieve. The filtered powder was then sieved using the fine mesh screen, removing the smallest particle sizes from the batch. The unfiltered particles were within the desired size range of 100 and 300 μm and were used during experimentation.

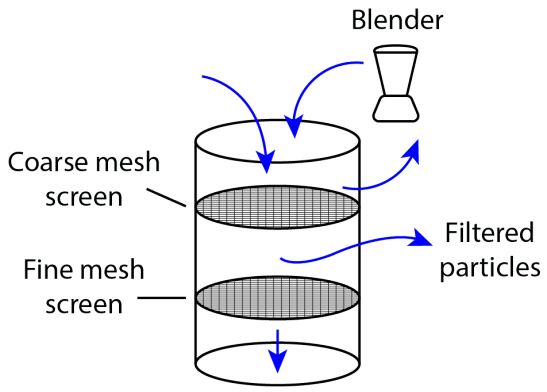


Figure 4.1 Powder sieving process using two mesh screens.

### 4.1.2 Granular Mixing Process

For the mixed 100/300 µm powder beds, five different concentrations of each particle were evaluated. The concentrations are 0%, 25%, 50%, 75%, and 100% 100 µm beads and are denoted by the relative weight percentage of 100 µm glass beads. A granular mixture of 0% 100 µm beads, for example, represents a powder bed consisting solely of 300 µm particles. At 25% 100 µm beads, it would be 25% 100 µm and 75% 300 µm glass beads respectively. To create the bimodal powder beds, the sieved 100 and 300 µm particles were weighed to their relative proportions at any given concentration and placed into a glass container. The container would be manually vibrated for one minute and dispensed onto petri dishes for static experimentation.

## 4.2 Liquid Selection

For the static experiments, the liquid chosen is a common polymer bonding agent consisting of hydroxy terminated polybutadiene (HTPB) resin, isodecyl pelargonate (IDP) plasticizer, and lecithin. The three substances were mixed in mass proportions 46% HTPB, 46% IDP, and 8% lecithin. This fluid combination was

chosen as it is already commonly used and studied in the energetics industry [14], [62]. In the dynamic experiments, silicone oil was used as the working liquid. The silicone oil was selected such that its viscosity would be similar to the polymer binder used in the static experiments. The change to silicone oil was to prevent any uncertainties in fluid properties and encourage the reproducibility of experimental results.

### 4.2.1 Viscosity Measurement

The viscosity of the polymer binder was determined using the AR2000 Rheometer with a cone and plate geometry. The rheometer produced shear rates in the range of 0.01-114 $s^{-1}$, shown in Figure 4.2, and revealed the dynamic viscosity of the polymer binder to be 0.52 Pa-s. The viscosity of the silicone oil was not determined experimentally. Instead silicone oil selected with kinematic viscosity of 600 cSt to closely match the viscosity of the polymer binder.

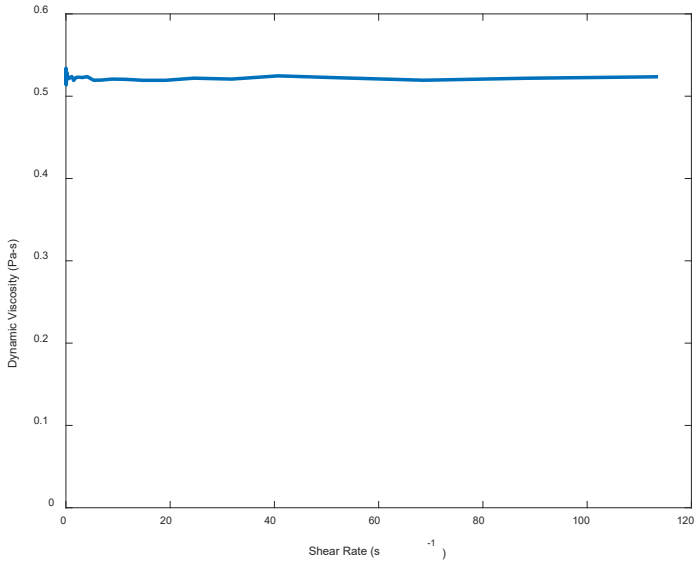


Figure 4.2: Rheology data of polymer binder under shear.

### 4.2.2 Surface Tension Measurement

The surface tension of both liquids was measured through a capillary tube experiment. In this experiment a capillary tube of known diameter is placed slightly under the liquid-surface level of a reservoir of liquid. Due to capillary action, the liquid climbs up the tube, up to a certain height signifying the balance between capillary forces and gravity. The surface tension can then be determined through a force balance equation. The setup of the capillary tube experiment can be seen in Figure 4.3.

$$2\pi r\gamma \cos\theta = \rho g h \pi r^2 \tag{4.1}$$

$$\gamma = \frac{\rho g h r}{2\cos\theta} \tag{4.2}$$

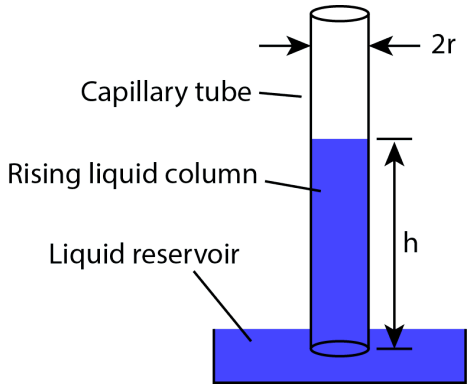


Figure 4.3: Capillary rise experiment

A capillary tube of 0.2 mm in diameter was used to carry out this experiment. The height of the liquid column for the polymer binder and silicone oil were 29.5 and 41.9 mm respectively. There was no noticeable contact between the liquid front and the wall, therefore $\cos\theta \approx 1$. Using the liquid heights and fluid properties of the

polymer binder and silicone oil in equation 4.2 gave surface tension measurements of 0.027 and 0.04 N/m respectively.

### 4.2.3 Contact Angle Measurement

Contact angle between the liquid mixtures and solid particles was determined through a Washburn capillary rise experiment. The powder was packed into a glass tube measuring 10 mm in diameter and submerged slightly under the liquid surface level of the reservoir with cotton acting as the permeable film separating the liquid and the powder. The change in mass of the liquid reservoir was recorded over a one-minute period. Using equations 3.9 and 3.10 in conjunction with the viscosity and surface tension measurements, the contact angle of the polymer binder on glass beads and granulated sugar was found to be 54º and 32º respectively. Likewise, the contact angle of the silicone oil on glass beads and granulated sugar was found to be 27º and 18º respectively.

# Chapter 5: Static Experimentation

Liquid-solid mixing consists of two steps: feeding liquid into static powder and dynamically mixing ingredients to homogenize the mixture. In order to determine the feed protocols for the dynamic experiments, static experiment is to determine the wicking and wetting behavior of liquids in various porous media. The depth at which fluid permeates the porous medium and the distance it spreads on the surface of the powder bed are vital in determining the initial position of ingredients within the powder bed, or the feed protocol. Fluid properties are already known, but what remains unknown is how the fluid will spread on a porous surface. In this chapter, the spreading of the fluid into the porous medium, through wicking and wetting, will be evaluated. The area that the fluid can fill gives insight into how the fluid must be fed and will be vital in the preparation of the feed protocol, or the placement of fluid within the porous material. The results of this experiment will lead to the development of a feeding protocol for initial charging of fluid within powder.

## 5.1 Wicking Characterization

The initial charging of the porous material is facilitated by above-surface method. The process involves dispensing fluid onto the powder surface. Under this process, fluid will spread on the powder surface and wick below the surface simultaneously [63]. Fluid flow above the surface will be denoted as wetting and flow below the surfaces as wicking. Fluid above the surface will radiate from the impact point. The wetted region formed using the above-surface dosing method spreads to a

diameter, *D*, on the surface and wicks the powder a distance, *L*, below the surface. The wicking depth can be modeled by the Washburn equation with maximum depth occurring at the center over the entire wicking time. The wetting diameter was determined through experimentation and affects the spacing of wet regions in the initial charging feed protocol.

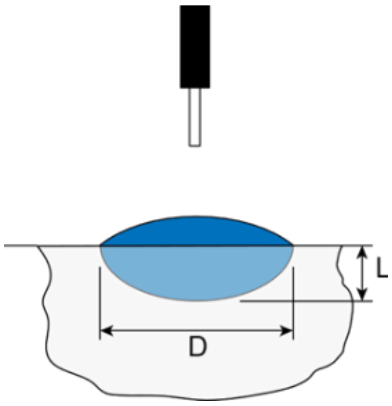


Figure 5.1: Above-surface dispensing method used in the initial charging feed protocol

In this preliminary experiment, the wetting diameter of polymer binder onto the surfaces of glass beads and granulated is recorded as a function of time. A total fluid volume of 1.5mL is dispensed onto the powder surface using an 18-gage needle positioned 20 mm above the powder surface and oriented completely normal to the surface plane. The liquid is dyed with AUTOMATE Blue liquid dye (<0.1g) to create good contrast with the white powder. As the liquid is dispensed onto the surface, the surface spreading is recorded with a stationary FLIR Chameleon3 camera at 30fps and resolution of 1.3MP. Experimentation with glass beads incorporated mixed compositions of both 100 and 300 µm particle sizes, with each composition being denoted by the concentration of 100 µm beads present. Experimentation with the

sugar did not utilized mixed compositions, using singular particle size powder beds. With these two powder bed types, it will be possible to determine surface spreading characteristics which will be useful in creating a liquid feeding protocol.

### 5.1.1 Image Processing of Wetting Diameter

The outcome of image processing is to extract the diameter of the wetted region for experimental footage as a function of time. Image processing occurs in a loop over each frame of the experimental video beginning with the frame immediately before the liquid stream is visible in the camera frame (i.e. a frame of the dry powder bed). In each frame, the diameter of the cylindrical container is visible and is used to determine the conversion factor from millimeters to pixels. The camera is stationary while filming, therefore the conversion factor needs to be calculated only once and can be done so at the first frame of the video. Each frame is converted from an RGB image to a grayscale image. Isolating the wetted region is done using the background subtraction technique, which can only be done if the background is stationary. The first frame of only dry powder is subtracted from each subsequent frame to show only the pixels that have changed in grayscale value. With a stationary view, the only changing pixels are those occupied by the wetted region. The resulting image is then converted to from grayscale to binary and the MATLAB function *conncomp()* can be used to determine shape properties of the region, such as the area and centroid. An image filtering function is also applied to remove noise from the image. A breakdown of the image processing can be seen in Figure 5.2 below.

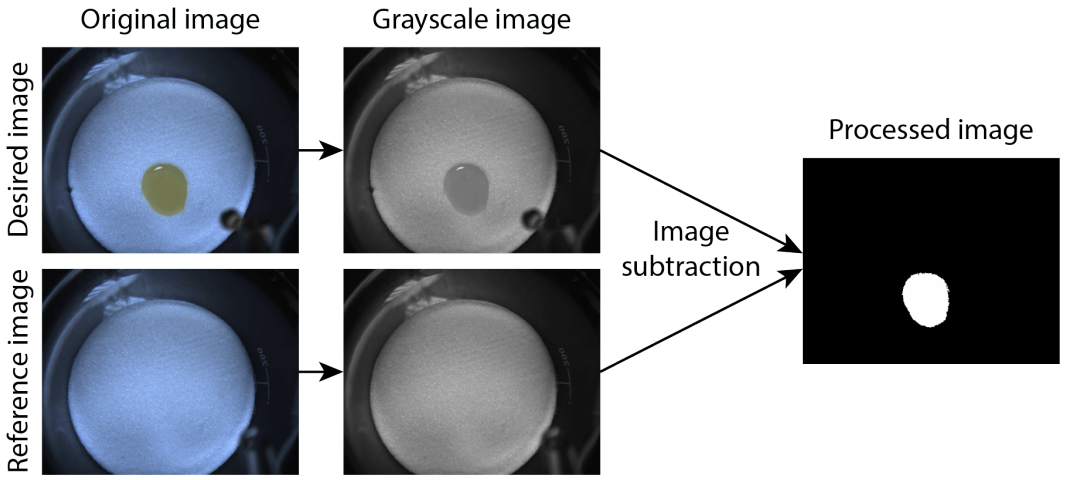


Figure 5.2: Background separation image processing technique for wetting diameter.

The area property of wetted region in each frame has units of $px^2$. This area is converted into $mm^2$ through the conversion factor, *c*, obtained earlier. The area of the wetted region is assumed to be circular, as such each instance of the wetted region's growth has an equivalent diameter, *d*, which can be calculated by equating the area of the region to the area of a circle. Over multiple timesteps, the wetting diameter growth can be determined using equations 5.1-5.3. A breakdown of the code used for image processing is presented in Appendix D.1.

$$c = \frac{d_{container\ (mm)}}{d_{container\ (px)}} \tag{5.1}$$

$$A_{mm^2} = c^2 A_{px^2} \tag{5.2}$$

$$d = \sqrt{\frac{4A_{mm^2}}{\pi}} \tag{5.3}$$

### 5.1.2 Wicking Behavior

Experimentation with the glass beads reveal the impact of free volume on the rate of above-surface wetting and wicking. Of the different compositions tested, the fluid dispensed onto a concentration of 50% 100 µm beads takes the longest time to asymptote to a constant diameter. This is explained by the porosity of the mixed batches. For uniformly round particles, the largest free volume occurs within powder beds consisting of a single particle size. For bimodal mixtures of uniformly round particles, the largest free volume occurs when the powder bed consists of a single particle size. With particles of different sizes, the free volume decreases and there exists a concentration at which free volume reaches a minimum. This concentration is near a 50% concentration of 100 and 300 µm glass beads [64]–[66]. This behavior is replicated as the feed rate increases from 0.15 to 0.3 mL/s as seen in Figures 5.3-5.5.

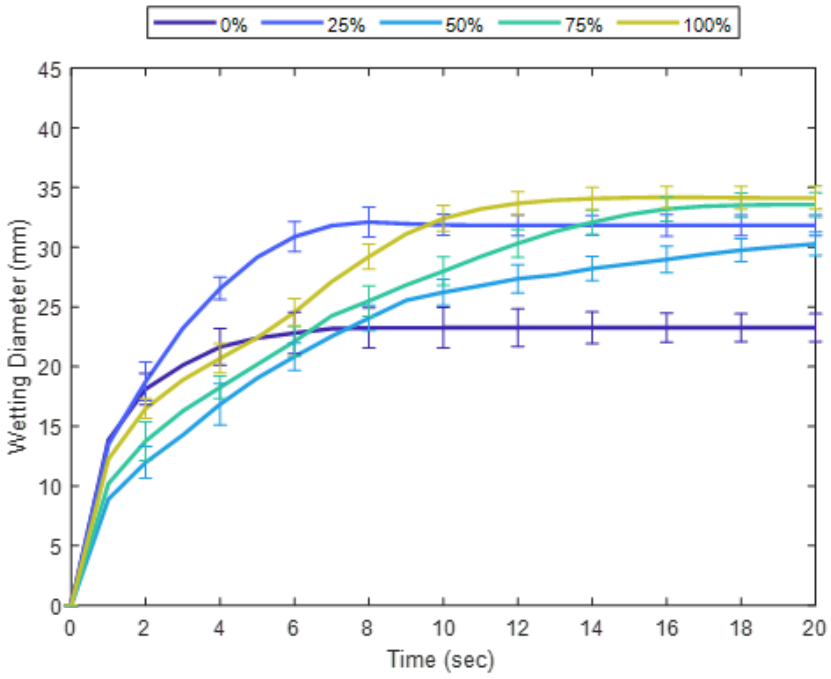


Figure 5.3: The spreading diameter growth on glass beads at 0.15 mL/s.

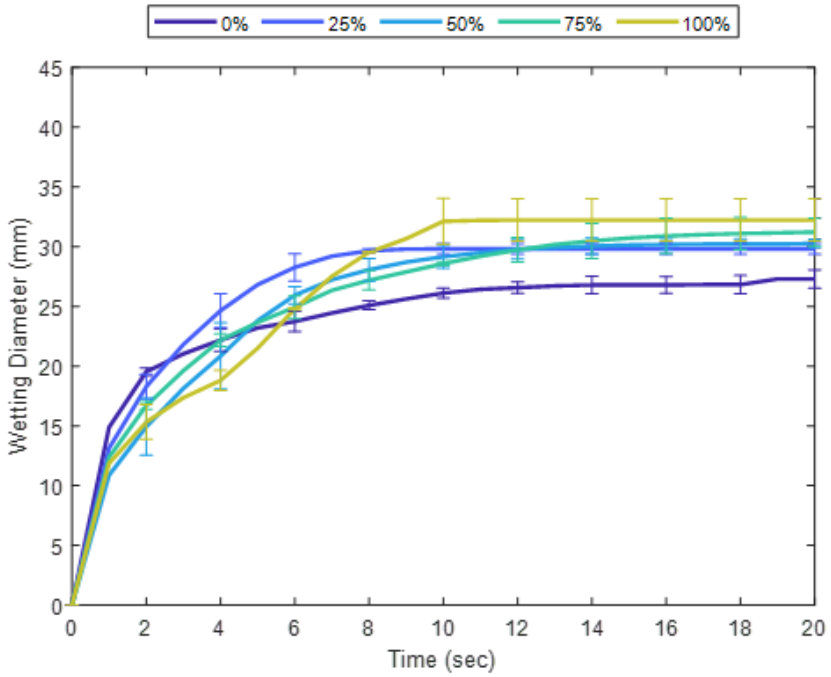


Figure 5.4: The spreading diameter growth on glass beads at 0.2 mL/s.

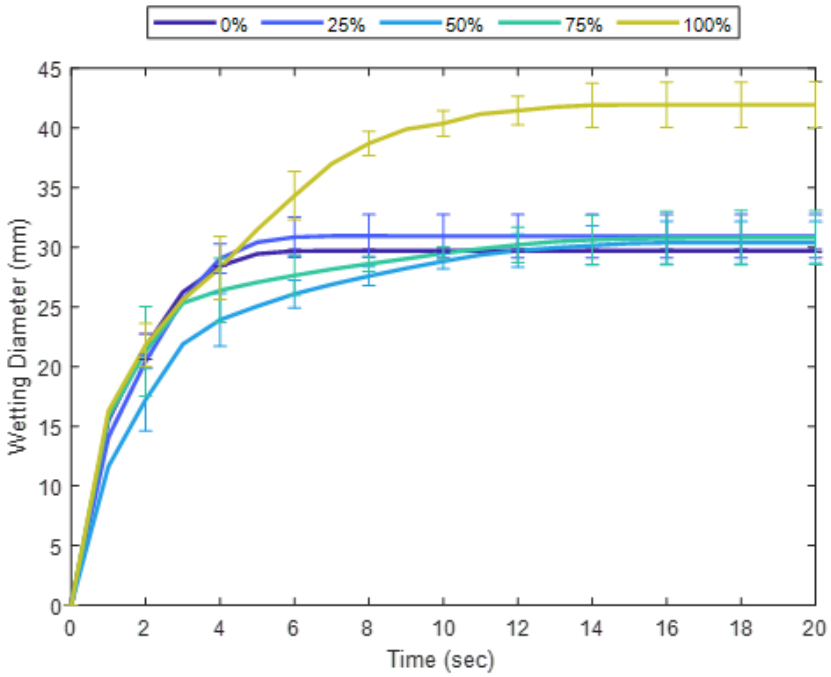


Figure 5.5: The spreading diameter growth on glass beads at 0.3 mL/s.

In these experiments the spreading diameter growth varied with feed rate and began to overlap one another as the feed rate was increased, as shown in Figures 5.3-5.5. This was observed among each of the mixed compositions as well as by the different sugar sizes shown in Figures 5.6 and 5.7. The overlap is caused by the powder's inability to absorb the fluid faster than the rate at which the fluid is dispensed. Fluid is absorbed into the powder at a known rate, given by the Washburn equation. A dispensing rate lower than the wicking rate results in higher wicking below the surface than wetting above. However, if the fluid is dispensed at a higher rate, fluid spreads above the surface at a greater rate, forming the wet agglomerate into a disk-shaped wet agglomerate. The boundary between both occurrences is the critical wicking rate and can be observed among the feed rates tested with the glass and sugar. For the glass the critical wicking rate lies between 0.2 and 0.3 mL/s. For the sugar, this critical wicking rate is found to be 0.2 mL/s for the 100 μm sugar and 0.3 mL/s for the 300 μm sugar.

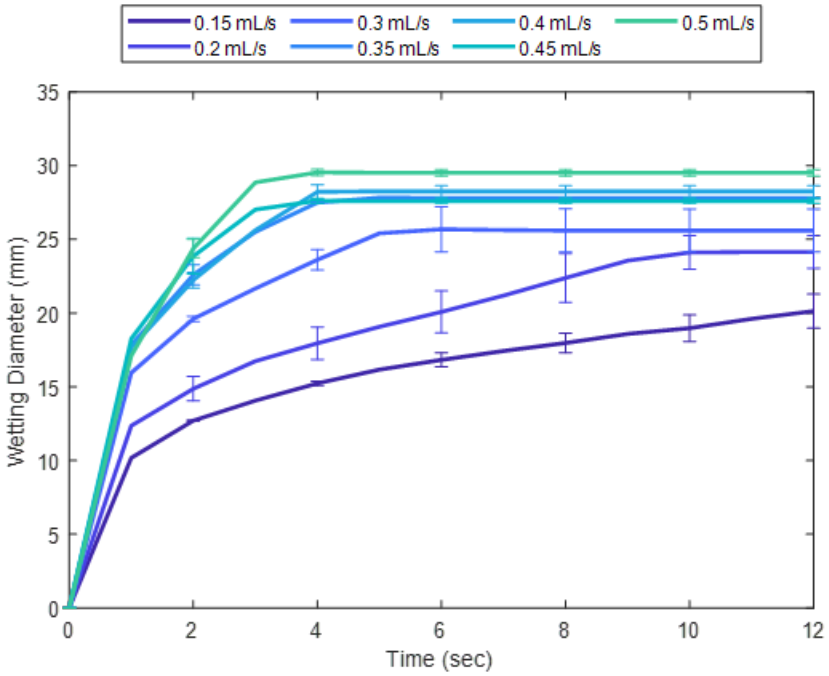


Figure 5.6: The spreading diameter growth on 300µm sugar.

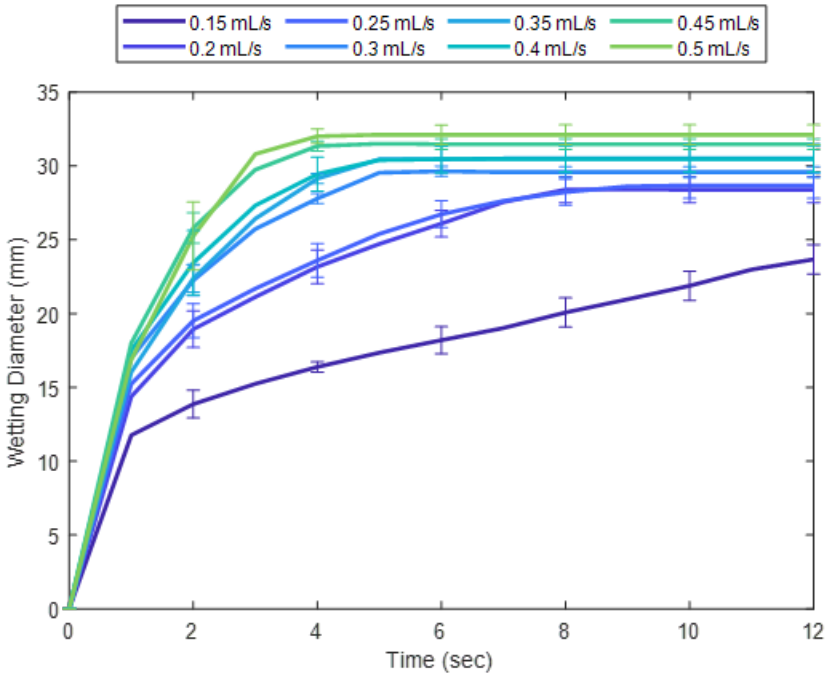


Figure 5.7: The spreading diameter growth on 100µm sugar.

## 5.2 Conclusions

We compared vertical addition of the fluid into the bed versus the addition on top of a bed. We found there was a larger volume of wetted beads in the latter method. In each of the tested conditions, the spreading of fluid on the surface as far larger than the wicking underneath. This means that the fluid is unlikely to wick across the entire depth of the container. In order to compensate for this and wet a large portion of the powder prior to vibration mixing, the fluid would need to be dispensed in layers. Through experimentation, the shape of the wetted region could be predicted given the particle size, fluid properties, and feed rate. This led to the discovery of critical feed rates that occur when the dispensing rate equals the wicking rate. At feed rates higher than this critical value, the surface spreading of liquid will grow at a fixed rate.

# Chapter 6: Dynamic Experimentation

An experiment is conducted to improve mix quality based on the loading procedure and the mixing parameters. The goal of this experiment is to determine a relationship between the measures of mixing and dynamic mixing parameters of acceleration and number of cycles. This relationship will be used to determine the effect mixing parameters have on the mixture. This will give insight into the forces at play within the mixer and establish a criterion for mixing to occur. We posit that the apparatus moves in a sinusoidal pattern. In between the changes in the direction, the wetted material and the dry material are moving at the same speed, the result of which is that there is no force imparted to the wetted blob. It is only in the changes of direction where the heavier wetted blob will move at a different speed from the dry particles and be able to impart a force. The magnitude of the acceleration is then related to the amount of force that is imparted to the wetted blob.

## 6.1 Experimental Apparatus

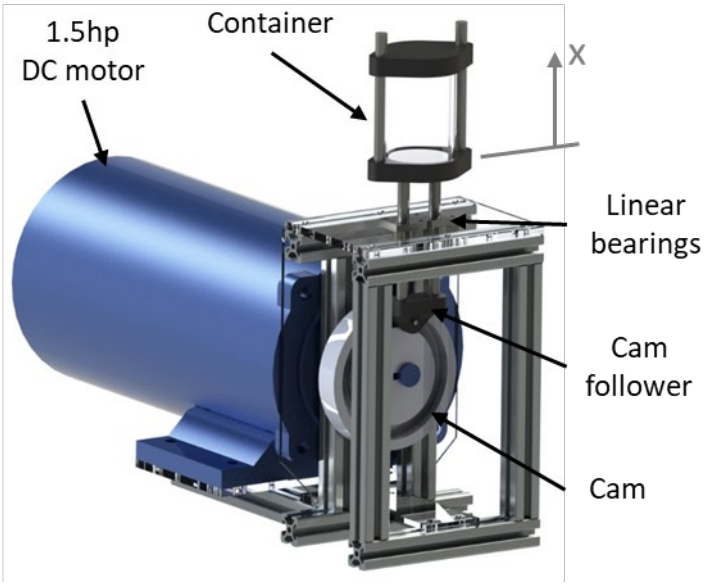


Figure 6.1: Experimental apparatus.

A custom mixer was made to facilitate the dynamic experiment mixing. The mixer oscillates the container of ingredients linearly in a sinusoidal path and has a max acceleration output of 15g's. The oscillating container is connected to a rotating cam by way of cam follower. Oscillations are fixed in the vertical direction by way of linear bearings. The cam controls the path of the mixing container, completing one sinusoidal period with amplitude of 10mm for every revolution of the cam. The cam is connected to a 1.5 hp DC motor with controllable rotational speed, $\omega$. The acceleration that the ingredients experience is determined by amplitude and rotational speed through the following equations:

$$x = A \sin \omega t \tag{6.1}$$

$$a = -A\omega^2 \sin \omega t \tag{6.2}$$

The number of mixing cycles is dependent on the frequency of rotation, $\omega$, and the time of mixing, $t$, through the following formula:

$$N = \frac{\omega t}{2\pi} \tag{6.3}$$

### 6.1.1 Manufacturing Process

The DC motor is held in place by a scaffolded structure made of aluminum slotted frames and acrylic panels. The acrylic panels are fastened onto the slots of the aluminum framing and act as gusset plates to the aluminum beams, fixing them in place. Two linear bearings are placed on the roof of the scaffold to allow the container to travel axially without transverse movement. The container is fixed to the vibrating stage with a clamping device. The two ends of the clamps are CNC machined from polyethylene sheets with circular indents for the glass container to rest on. The top clamp is able to slide on a pair of rods and can be fixed through friction fitting via set screws at each end of the clamp.

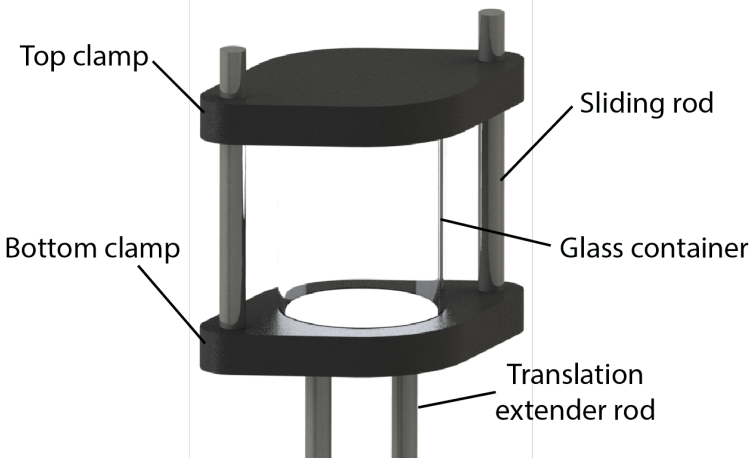


Figure 6.2: Container clamping structure.

Attached to the container is the cam follower. The cam follower measures 10 mm in diameter and is attached to an intermediary structure simply called the cam bridge. The purpose of this structure is to enable translation of the container through the cam follower. The cam bridge fixes the translating rods with set screws and has mounting space for the cam follower. This component was 3D printed out of carbon fiber filament through the fused disposition modelling (FDM) process.

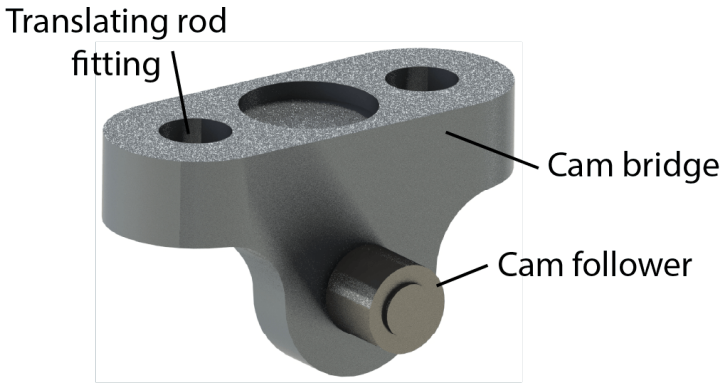


Figure 6.3: Cam bridge assembly.

As stated earlier, the cam facilitates the sinusoidal motion of the container. The specification of the cam pathway is to complete one sinusoidal period after each rotation. The amplitude of vibration was chosen to be 10 mm. With an amplitude constraint of 10 mm and the radial offset from the pivot, $r_{off}$, the cam path equation could be determined and is listed as equation 6.5. The cam was modeled in Solidworks and CNC machined with a DATRON Aluminum CNC Router. A tolerance of 0.1mm was added to the path to allow for smooth rotation of the cam follower.

$$r_{cam} = r_{off} + A\sin(\theta) \tag{6.4}$$

$$r_{cam} = 37 + 10\sin(\theta) \tag{6.5}$$

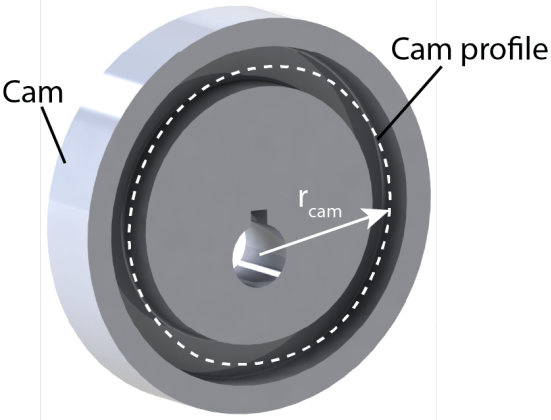


Figure 6.4: Cam rotating element.

### 6.1.2 Motor Sizing

The power requirements of the motor depend on the mass of the ingredients and container, as well as the geometry of the cam itself. A force balance of the oscillating container is used to determine the mixing force, $F_{mix}$, necessary to move the container at the specified acceleration in equation 6.7 under the effect of gravity.

$$\sum F_x = ma = F_{mix} - mg \tag{6.6}$$

$$F_{mix} = m(g - A\omega^2 \sin(\omega t)) \tag{6.7}$$

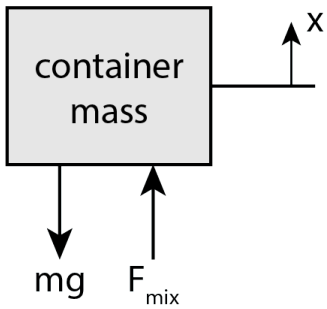


Figure 6.5: Free body diagram of oscillating container.

The mixing force represents the x-direction force supplied by the motor and occurs at the contact point between the cam follower and the walls of the cam pathway. Assuming the mass of the cam follower to be negligible, the mixing force can be written in terms of the normal force, $F_N$, exerted by the cam walls and the angle, $\alpha$, between the normal force and mixing force.

$$F_{mix} = F_N \cos \alpha \tag{6.8}$$

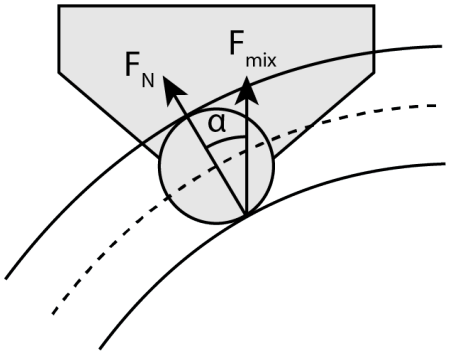


Figure 6.6: Free body diagram of cam and cam follower collision.

By using the position of the cam relative to the cam pivot $r_{cam}$ found from equation 6.5, the geometry of the curved surface the lever arm, $r_T$, perpendicular to the normal force can be calculated using:

$$r_T = r_{cam} \sin \alpha \tag{6.9}$$

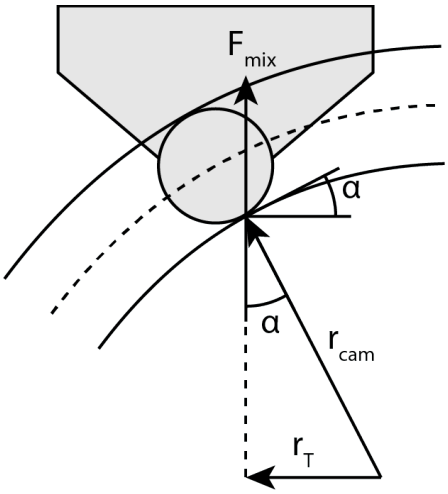


Figure 6.7: Geometric relationship between cam profile and mixing force lever arm.

Combining equations 6.8 and 6.9 gives required torque of the motor as:

$$\tau_{motor} = F_N r_T \tag{6.10}$$

$$\tau_{motor} = F_{mix} r_{cam} \tan\alpha \tag{6.11}$$

Geometry wise, $\tan\alpha$ is the tangent of the contact surface of the cam wall and cam follower. This is equivalent to the velocity of the cam follower and can be substituted into equation 6.11, along with expressions for $F_{mix}$ and $r_{cam}$, to give a final solution for $\tau_{motor}$ and $P_{motor}$ as:

$$\tan\alpha = \frac{dx}{dt} = A\omega\cos(\omega t) \tag{6.12}$$

$$\tau_{motor} = mA\omega\cos(\omega t)\,(g - A\omega^2\sin(\omega t))\big(r_{off} + A\sin(\omega t)\big) \tag{6.13}$$

$$P_{motor} = mA\omega^2\cos(\omega t)\,(g - A\omega^2\sin(\omega t))\big(r_{off} + A\sin(\omega t)\big) \tag{6.14}$$

The desired peak acceleration is 15 g, resulting in a value for $\omega$ as 121.3 rad/s when oscillating at 10 mm amplitude. A container mass of 300 g was used to simulate

high container fill. Substituting values for $g$ and $r_{off}$ into the power equation gives motor power requirement over a single oscillation. The peak power requirement of $P_{peak} = 0.89\ hp$ was found at. Given these power and angular frequency requirements, a 1750 rpm, 1.5 hp DC motor was selected to facilitate liquid-powder mixing.

### 6.1.3 Digital Control

The acceleration and number of mixing cycles are the two controllable inputs to vibration mixing. The number of cycles is controlled by the apparatus through an Arduino microcontroller. The microcontroller acts as a switch for the motor power input. Values for acceleration, a, and number of cycles, $N$, are entered into a script. The script controls the rotational speed of the motor, $\omega$, to produce the set acceleration and the time duration, $t$, for the motor switch to correspond to the set number of cycles. This is achieved by the following formulas:

$$\omega = \sqrt{\frac{a}{A}} \tag{6.15}$$

$$t = \frac{2\pi N}{\omega} \tag{6.16}$$

### 6.1.4 Harmonics Testing

The mixing apparatus must oscillate at the prescribed accelerations to provide reliable data for dynamic testing. To this end, harmonics testing of the apparatus is used to isolate the frequencies of the system and ensure that accelerations in transverse directions are not significant. Accelerations in the x, y, and z-directions

will be measured with an Adafruit ISM330DHCX accelerometer with a sampling frequency of  and controlled by an Arduino Uno microprocessor. The accelerometer is mounted on the top clamp of the clamping system and is oriented such that the z-axis is parallel to the vertical oscillations of the device. In this test, accelerations of 2.5, 5, 7.5, 10, and 12.5 g of will be tested. These accelerations correspond to the dynamic testing conditions to be covered in the next section. The sensor produces signals like the one shown in Figure 6.8.

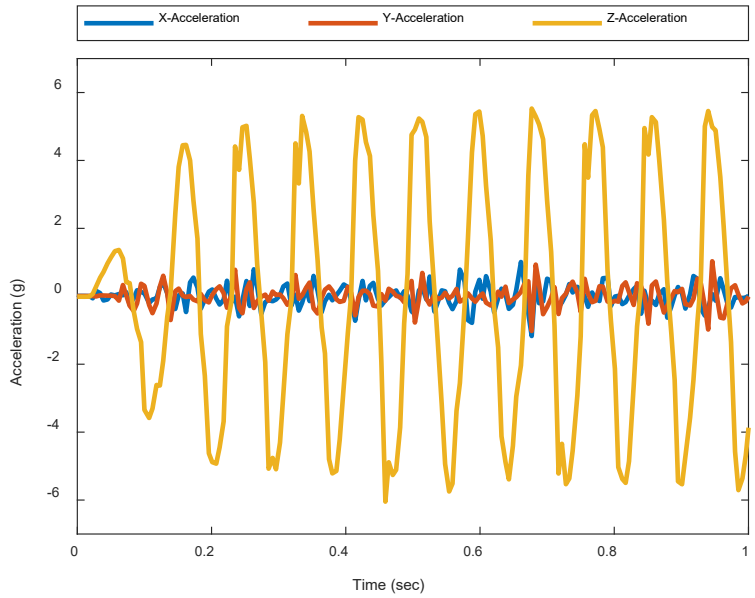


Figure 6.8: Acceleration response in x, y, and z-directions at 5 g.

The signal is composed of many frequency components. These components carry their own energy signatures and can be isolated through a spectral density analysis of the signal. This process decomposes the signal into a number of discrete frequencies through a Fourier transfer. The energy spectra at each acceleration are shown in Figures 6.9-6.11.

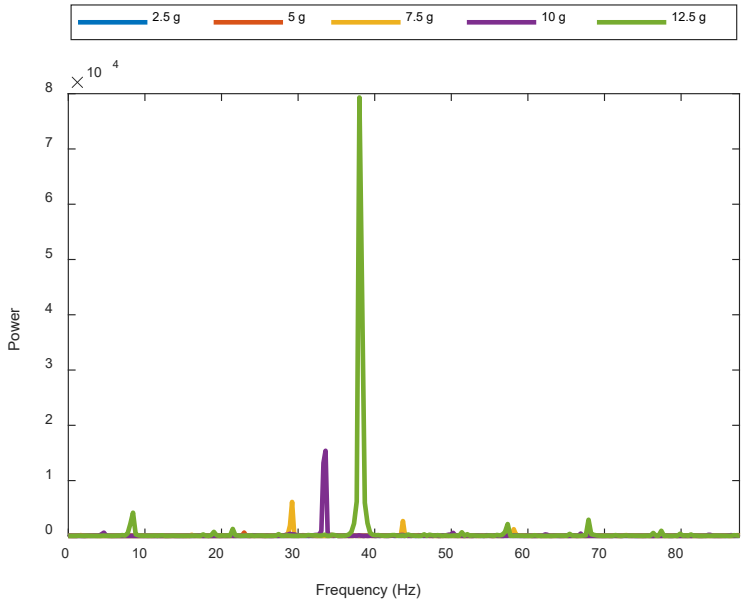


Figure 6.9: X-acceleration frequency energy spectrum.

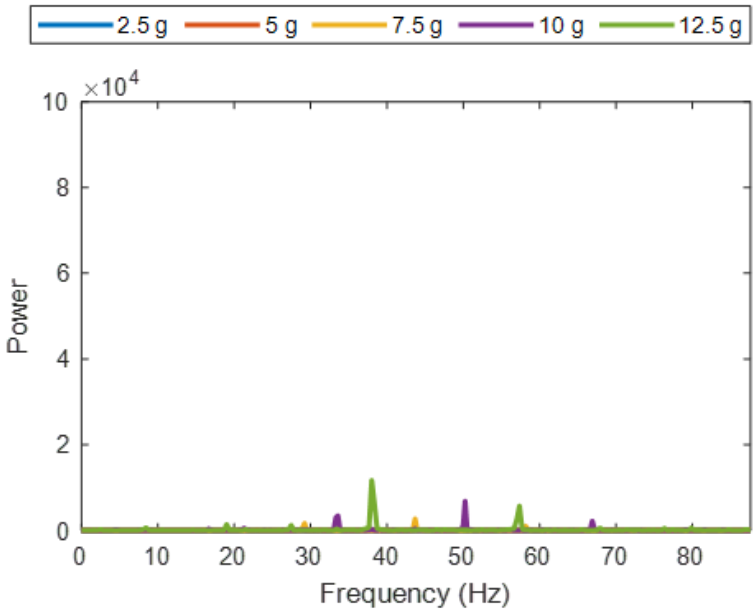


Figure 6.10: Y-acceleration frequency energy spectrum.

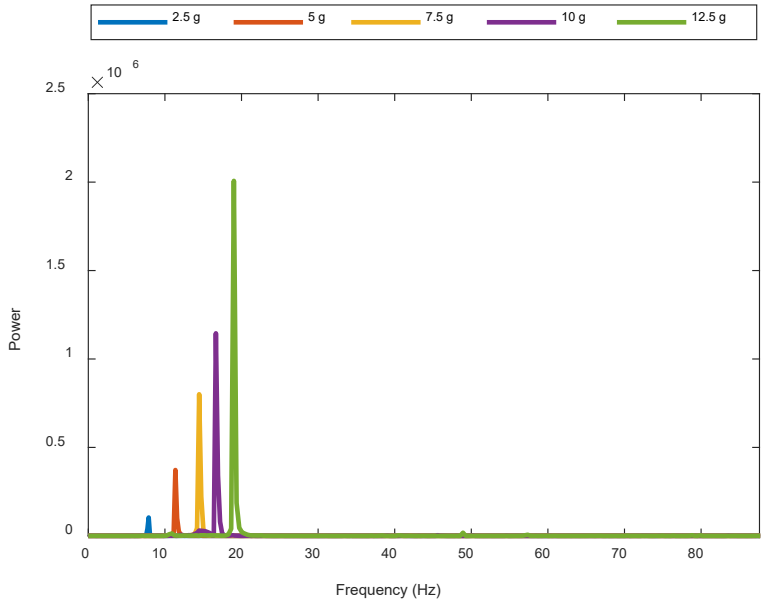


Figure 6.11: Z-acceleration frequency energy spectrum.

From the spectral analysis, the Z-acceleration is found to carry the highest energy. Although not insignificant, the accelerations in the x and y-directions are several orders of magnitude smaller than the acceleration in the z-direction. Therefore, excitation of the powder from the x and y-accelerations is considered negligible. The energy spectrum for z-accelerations reveal that there is a single dominant frequency at each mixing acceleration, and that frequency corresponds to the excitation frequency of the vibrating platform. The excitation frequencies are found to be 7.9, 11.1, 13.7, 15.8, and 17.6 Hz for 2.5, 5, 7.5, 10, and 12.5 g accelerations respectively.

## 6.2 Design of Experimentation

In this experiment, 5.56g of 600cSt silicone oil and 78.16g of 300µm glass beads were loaded into glass containers. The volume of liquid used represents 1/3 the

void space of close-packed solid particles. The addition of the fixed liquid volume had to follow the following rules: 1) the liquid would be placed horizontally on top of a each layer; 2) the space between layers were on the order of the wicking length and the maximum container amplitude; and 3) the wetted bed could not touch the container walls. The liquid was split equally into 4 layers each spaced 6mm apart within the powder bed. This was done by feeding a layer of powder then liquid directly above it using the above-surface dispensing method. This was repeated 4 times and topped with a final layer of powder. Four layers are chosen because it is the minimum number of layers required before the liquid reaches the walls. It is very important to make sure that the fluid does not touch the walls as contact adds an additional resistive force that must be overcome to cause motion of ingredients in the mixer. This resistive force is difficult to overcome at lower accelerations.

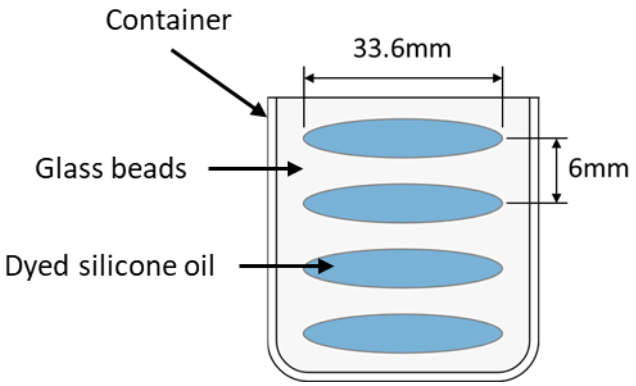


Figure 6.12: Four-layered feeding protocol

The variables for experimentation included 1) the acceleration of the mix and 2) the number of cycles of mixing. A Central Composite Design (CCD) Grid was used to evaluate the performance of the mixture and determine an empirical relationship between the mixing result and the inputs of acceleration and number of

cycles. Acceleration, a, ranged from 2.5-12.5g's and number of cycles, N, ranged from 50 to 1050 cycles. These range of values were chosen because it covers the entire range of mix quality from not being well mixed to being very well mixed.

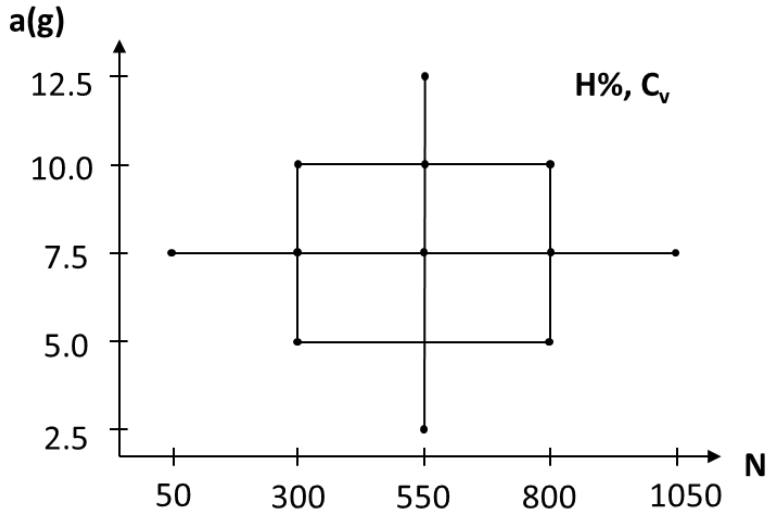


Figure 6.13: CCD Grid template with acceleration and mixing cycle dependencies.

### 6.2.1 Image Acquisition

To evaluate the distribution of ingredients within the mixture, it was imperative that the mixture could be removed from its container without disturbing its structure. A 3-dimensional representation of the structure can be done by splitting the sample into layers. A custom-built container was made to house the ingredients during mixing and allow for easy extraction once mixing was complete. The container consisted of a glass tube with two detachable lids on either end. The container measured 47mm in diameter and 60mm in height internally. Upon termination of mixing, the container would be removed from the mixing apparatus and the top lid would be removed. A 3D printed piston, with diameter equal to the internal diameter of the glass tube, would be inserted through the top opening. The

piston is pushed into the container until it touches the top surface of the liquid-powder mixture. O-rings attached to the piston prevent glass beads from escaping the container. At this point the container is flipped upside-down and the bottom lid can be removed. The piston is pushed in 2mm increments. As the cylindrical sample rises above the top of the glass tube, music wire is used to slice the sample using the top circular edge of the tube as reference, leaving a flat surface. The surface is then photographed in a lightbox with constant illumination. Through repeated operation, a 3-dimensional image of the sample can be produced. The process is illustrated in Figure 6.14 below.

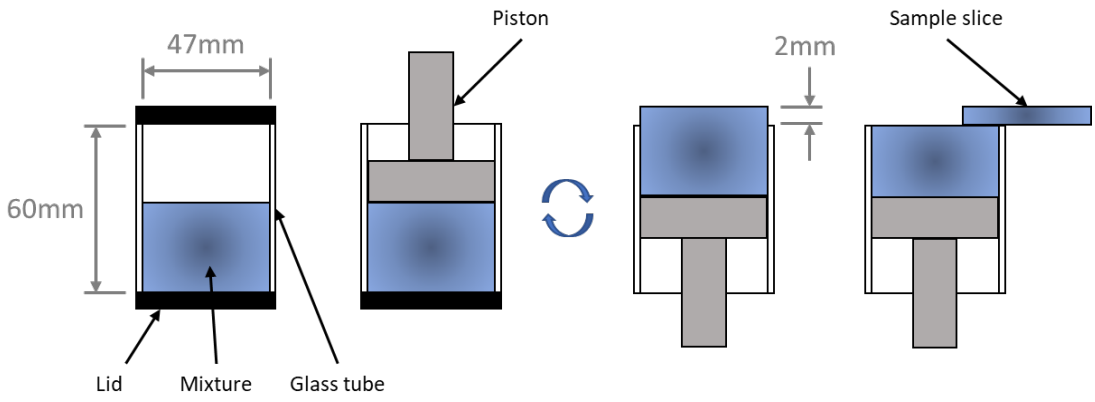


Figure 6.14: Sample acquisition procedure.

### 6.2.2 Image Processing of Mixing Measures

Like with the static experiments, images of the sample cross-sections show the entire circular region in order to obtain the conversion factor $c$. In order for the percent homogeneity and coefficient of variation to be calculated, a micropixel size must first be established. A study was conducted to determine the effect of macro pixel size on the perceived measures of mixing. The macro pixels ranged in square side-length from 1 to 10mm. The conversion factor was used to determine the

equivalent side-length in pixels. At each macro pixel size, $N$ grayscale macro pixels were extracted from the slice images. Each macro pixel is a $n \times n$ square array of grayscale values representing the concentration of liquid. Only the macro pixels within the container boundary were considered. Following the process for percent homogeneity and coefficient of variation, the average standard deviation and average value of all macro pixels was determined with the *std()* and *mean()* functions respectively.

The randomized version of each image was obtained by first reshaping the macro pixels into a $Nn \times 1$ one-dimensional array. The function *randsample()* sampled each pixel value randomly and created an array of randomized pixels. This new array was reshaped into $N$, $n \times n$ macro pixels to create the randomized version of the slice image. Values for $H\%$ and $C_v$ could now be obtained at each micropixel size by using equations 3.34-3.38. A breakdown of the code used to evaluate the measures of mixing can be found in Appendix D.2.

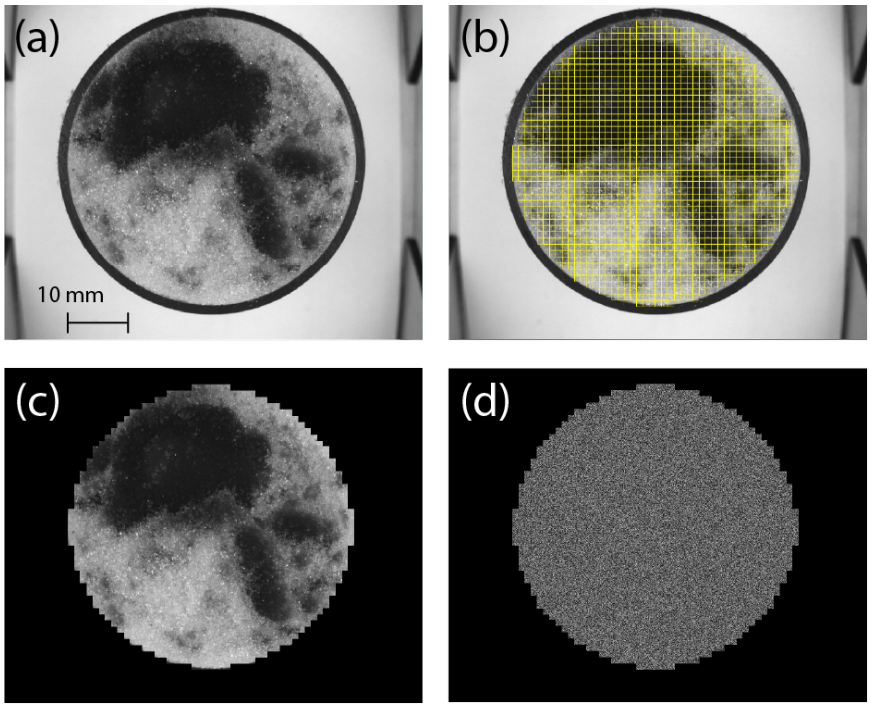


Figure 6.15: Image processing procedure. (a) grayscale image, (b) binning array, (c) binned image, and (d) randomized image

Percent homogeneity values are at their lowest in macro pixel sizes less than 1mm. At around 2mm side length, the processed value for percent homogeneity remains constant and slowly increases as the macro pixel size increases. The size of the macro pixels is usually dependent on the scales of mixing on is trying to achieve. In the case of liquid-powder mixing for pharmaceutical and energetic industries, smaller macro pixel sizes will provide better detail of mixing quality at small length scales. For this reason a 2mm macro pixel will be used for percent homogeneity and coefficient of variation estimates.

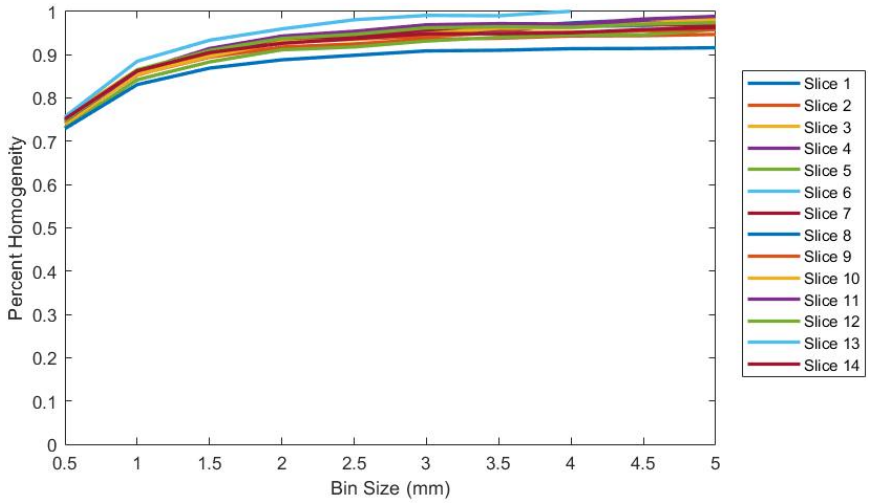


Figure 6.16: H% fluctuation as a function of bin sizefor N=1050 and a=7.5.

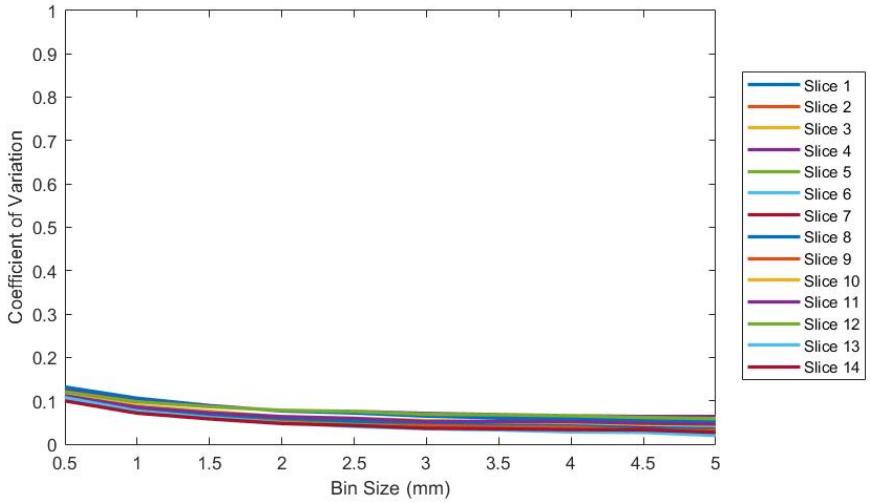


Figure 6.17: $C_v$ fluctuation as a function of bin size for N=1050 and a=7.5.

## 6.3 Liquid Dispersion and Breakup Modes

The images acquired through testing represent the distribution of liquid throughout the porous medium. The highest concentrations of liquid seen in the sample images are the remnants of the initial agglomerate. By isolating these high-concentration regions, it is possible to determine the amount of liquid that has

dispersed into the dry porous medium through a conservation of volume between the initial and final high-concentration volumes.

$$V\% = \left(1 - \frac{V_{final}}{V_{initial}}\right) \times 100\% \tag{6.17}$$

The images also allow us to evaluate the modes of agglomerate breakup at each operating condition. The fragments of the initial agglomerate have varying sizes and shapes post-mixing. The volume of the agglomerates in relation to the initial volume reveal the dominant breakup mode. For example, a fragment 1/3$^{rd}$ the size of the initial agglomerate is a clear indication of rupture whereas a fragment 1/100$^{th}$ the initial size indicates erosion. The dominant breakup modes will provide insight into the mixing forces exerted on the agglomerate, as well as the dependence of rupture and erosion on mixing parameters of acceleration and number of mixing cycles.

### 6.3.1 Image Processing of Percent Liquid Dispersion

The darkest regions of the cross-sectional images signify fragments of the initial agglomerate. The total volume of undispersed liquid is obtained by summing the volume of each individual fragment. Thus, the first step in image processing is to isolate the darkest regions from everything else. This is done through binary filtering and requires a grayscale value for thresholding light and dark regions. During image acquisition, images were taken in a controlled lighting environment via a lightbox. This means that the undispersed fragments appear as the same color in all the images and therefore a single threshold value can be used during image processing. A grayscale threshold value of 57 was used to separate the undispersed fragments in each cross-sectional image suing the *imbinarize()* function. Only pixels within the

boundary of the container were considered. The result is a series of binary images, one for each slice. The binary images are merged to create a 3-dimensional matrix thereby reconstructing the slices into a 3-dimensional view of the undispersed fragments.

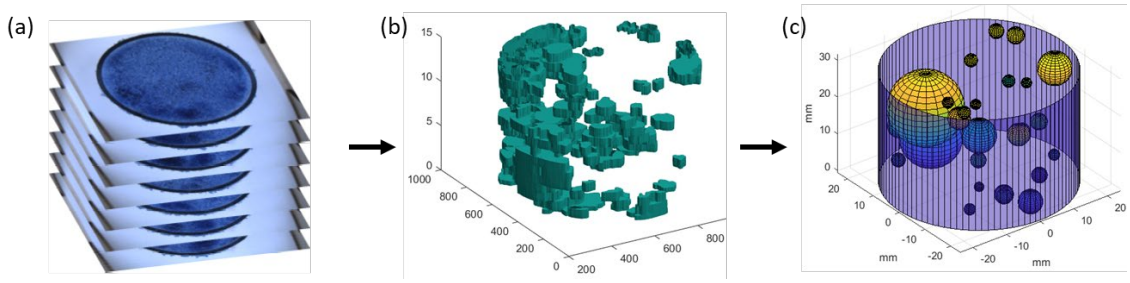


Figure 6.18: Image processing procedure from (a) cross-sectional image acquisition, (b) saturated region segmentation, and (c) simplification of connected components.

At each height of the matrix, there are areas illustrating the cross-sections of the fragments themselves. Regions that overlap between sequential heights are slices of the same fragment. The function *conncomp()* is used to connect overlapping regions into a single volume. When used on a 3D matrix, the function can determine the volume and centroid of each fragment. The conversion factor $c$ determined during the measure of mixing is useful in converting the $x$ and $y$ dimensions of the matrix from pixels to millimeters. The $z$ dimension of the matrix has a different conversion factor, $c_z$, and is the distance between slices. These two conversion factors can now be used to find the volume of each fragment using the following formula:

$$V_{mm^3} = c^2 c_z V_{px^3} \tag{6.18}$$

Summing the fragment volumes gives us the total undispersed volume after mixing. Plugging this value into equation 6.18 will calculate the percent liquid

dispersion for the specified experimental condition. A breakdown of the code used to evaluate the measures of mixing can be found in Appendix D.3.

### 6.3.2 Equivalent Fragment Diameter

Like with the spreading diameter, an equivalent diameter can be obtained for each of the undispersed fragments. The equivalent diameters will be used to compare fragments sizes an identify the presence of erosion and/or rupture breakup modes. The fragment volumes obtained in the previous step can be equated to the volume of a sphere and the equivalent diameter, $d$, can be found using:

$$d = \sqrt[3]{\frac{6V_{fragment}}{\pi}} \tag{6.19}$$

## 6.4 Results and Discussion

Data was generated by slicing mixed samples and measuring mix quality using image processing means. The slices measure 47 mm in diameter, and at that length scale the increase in acceleration and number of cycles improved the quality of the mixture. The percent homogeneity and coefficient of variation for the mixture across the range of mixing parameters were obtained as shown in Figures 6.19 and 6.20. The 30th, 60th, and 90th percentiles are used to categorize experimental samples based on their mixing performance and are represented as dashed lines on the CCD grids. Thus, the percentiles refer to sets of diagonals on the CCD grid. The results show that H% increases with acceleration and cycles whereas Cv. decreases with acceleration and cycles. For example, at a(g)=7.5, the %H increases from 31% to 93% as the number of cycles increases from 50 to 1050 cycles. Similarly, at a

constant 550 cycles, the acceleration is increased from 2.5 to 12.5 g. The %H increases from 37% to 90%. The trend also appears to be linear in natures as the diagonals of the CCD plots have very similar values.

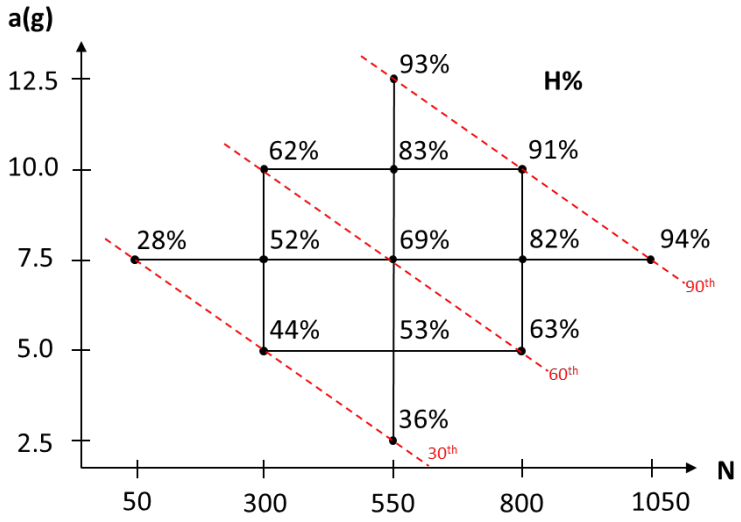


Figure 6.19: Percent Homogeneity surface response grid.

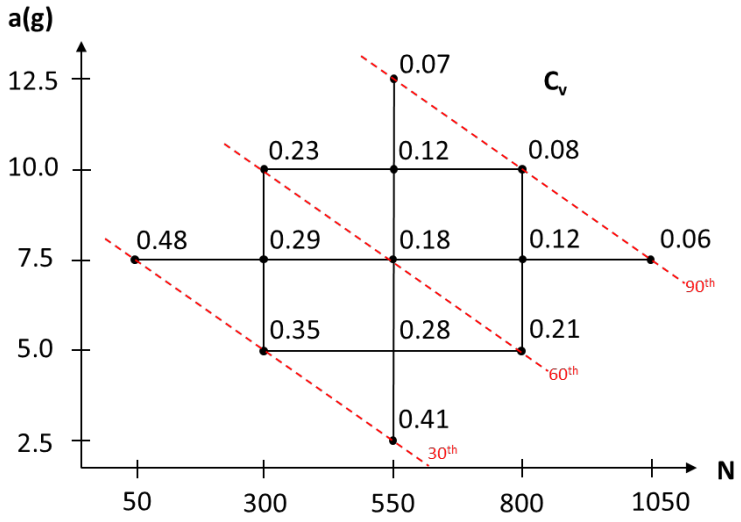


Figure 6.20: Coefficient of Variation surface response grid.

The CCD grids were analyzed using commercial software JMP Pro 14 to determine dependence of the measures of mixing on a, N, and higher orders. The

analysis shows a clear dominance (p-value<0.001) of first-order terms a and N, but very little effects from second order terms $a^2$, $N^2$, and $aN$. Results of this analysis are shown below:

$$H\% = 0.690 + 0.150\bar{N} + 0.123\bar{a} \tag{6.20}$$

$$C_v = 0.176 - 0.086\bar{N} - 0.067\bar{a} \tag{6.21}$$

$$\bar{N} = \left(\frac{N - 550}{250}\right) \tag{6.22}$$

$$\bar{a} = \left(\frac{a - 7.5}{2.5}\right) \tag{6.23}$$

| Source | LogWorth | PValue |
|---|---|---|
| Number of Cycles(300,800) | 3.641 | 0.00023 |
| Acceleration(5,10) | 3.415 | 0.00038 |
| Number of Cycles*Number of Cycles | 1.314 | 0.04858 |
| Acceleration*Acceleration | 0.864 | 0.13665 |
| Number of Cycles*Acceleration | 0.529 | 0.29578 |

Figure 6.21: Effect summary of surface response design outputted by JMP Pro 14 software.

As stated, the equations for percent homogeneity and coefficient of variation are linearly dependent on acceleration and number of cycles. We can also see that N is the dominant term in the equation as it is paired with the larger coefficient in both equations. In terms of mixing dynamics, the effect of the number of cycles is demonstrated in two ways. The first is the natural wicking that occurs between the liquid and powder. As illustrated by the Lucas-Washburn equation, wicking depth is proportional to time elapsed. At large number of cycles, more time has passed therefore liquid has penetrated more open pores, creating a better mixture. The second

is increased collisions. At each collision between the wet and dry particles, there is some transfer of fluid to the dry particles. Acceleration increases the amount of excess fluid and cycles increases the frequency. Having more collisions increases homogeneity and reduces variance.

### 6.4.2 Breakup Mechanisms: Experimental Observations

Mixing at low accelerations (up to 15g's) is done to better grasp the onset of particle breakup in a liquid-powder mixture through observable dispersion and distribution of agglomerates. The darker regions of the slices represent remnants of the original wet agglomerates, these are called the satellite drops. In Figure 6.22 below, samples in the 30th percentile tend to have the largest and most amount of satellite drops while those in the 90th percentile the smallest and fewest. We observe that the smallest of the satellite drops have a common size over the entire range of conditions. These daughter drops are about 3 mm in size and are present in all samples. The daughter drops signify the erosion process of the agglomerate. Until the threshold has been reached for agglomerate breakup, weaker portions of the agglomerate, such as those on the outer surface, will break off first. This is not so much a function of cycles, but purely of acceleration. The entire range of accelerations tested are able to overcome the weak adhesion force of the daughter drops.

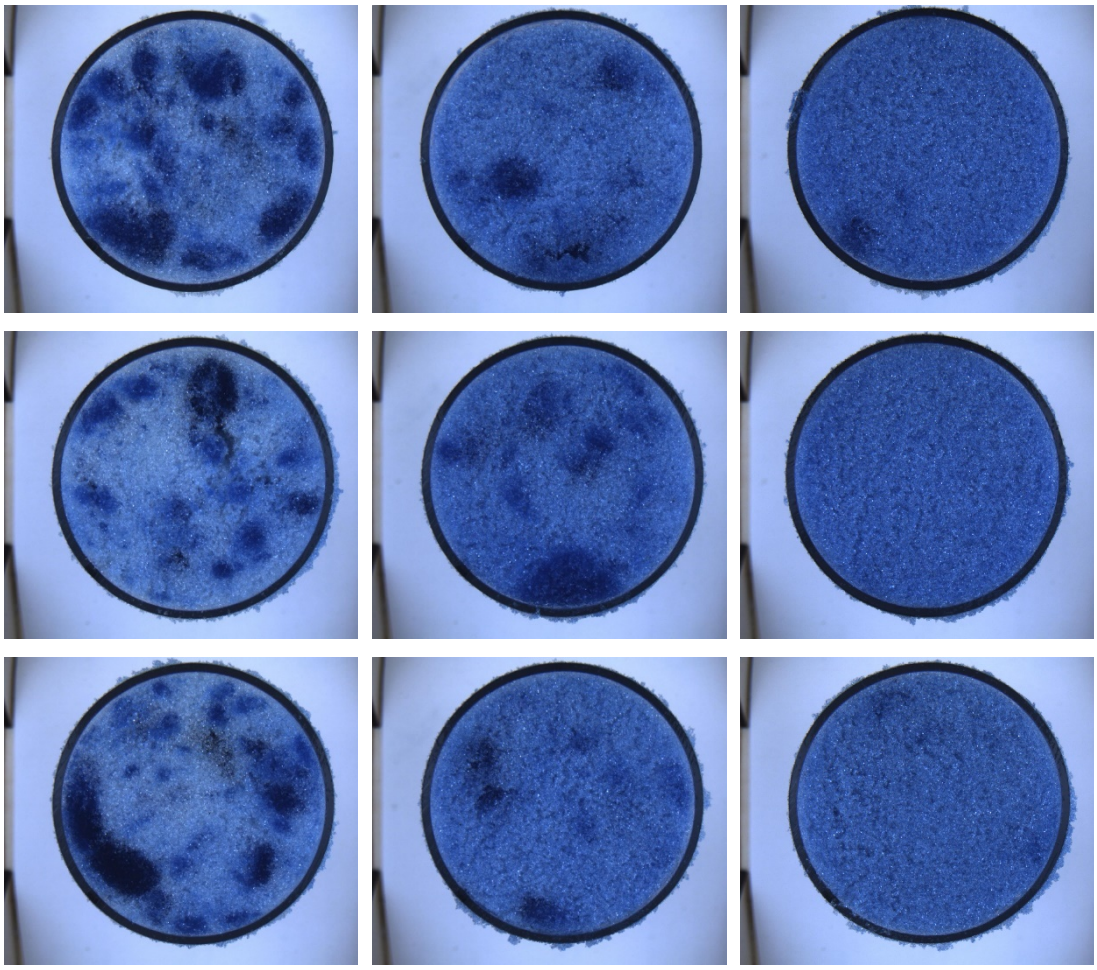

(a) (b) (c)

Figure 6.22: Cross-sectional slices of experimental samples at (a) 30th, (b) 60th, and (c) 90th percentiles.

The satellite drops, however, do not have a common characteristic size. They fluctuate is size from much larger than the initial disk-shaped agglomerate to a size comparable to the daughter drops. Samples from the 30th percentile tend to have the largest satellite drops. The size of these aggregates is much larger than any of the initial disk as illustrated by the 3D images in Figure 6.23. Despite having the four agglomerates separated initially, they merge into a single mass early in the mixing process. Additionally, satellite drops do not appear to break in halves. Agglomerate

dispersion at the 60th percentile, for example, shows a range of satellite drop sizes. If the satellite drops were derived from equal splitting of the initial agglomerate, then the satellite drops would have similar sizes throughout the mixing process. This phenomenon can be explained by the presence of the daughter drops and erosion. Erosion will gradually remove material from the initial agglomerate, therefore equal divisions of the agglomerate after erosion will never be the same size as equal divisions of the initial agglomerate without erosion.

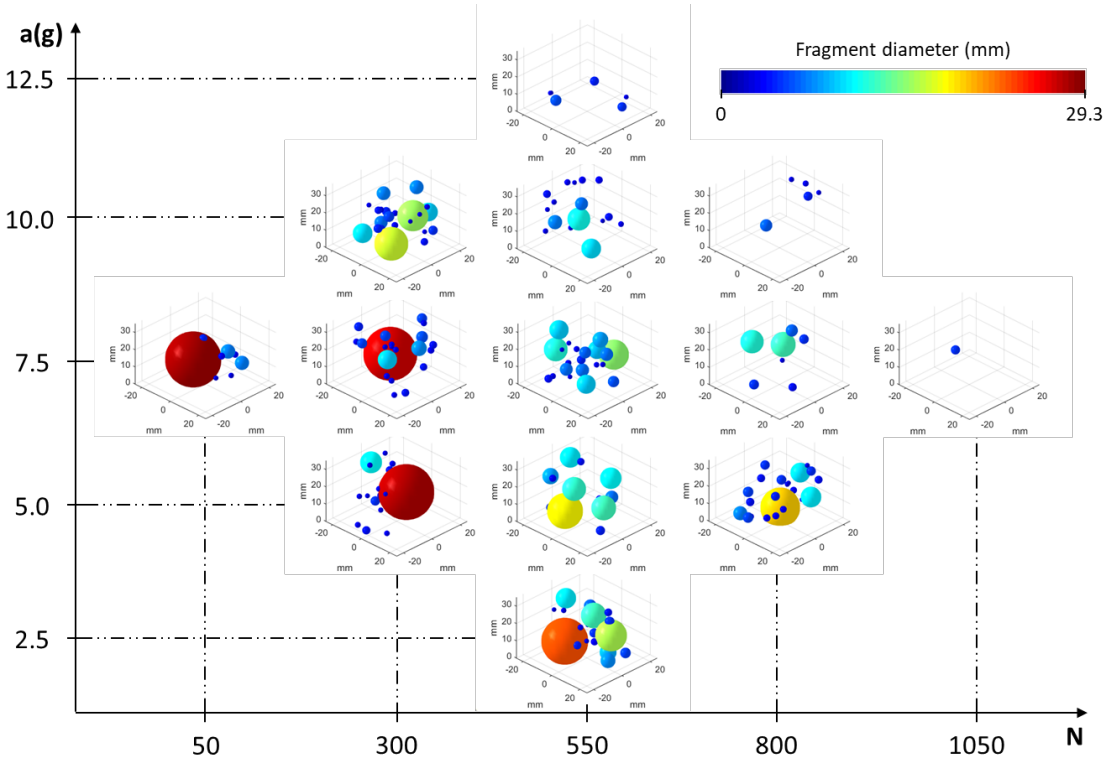


Figure 6.23: Agglomerate dispersion within the porous medium.

### 6.4.3 Breakup Mechanisms: Percent Liquid Dispersion

Liquid dispersion is evaluated from the 3D images at each experimental condition. This value reveals the extent to which the agglomerate has broken apart and dispersed into the porous medium. Using the process illustrated in section 6.3.1,

the percent liquid dispersion was obtained for each experimental condition shown in Figure 6.24.

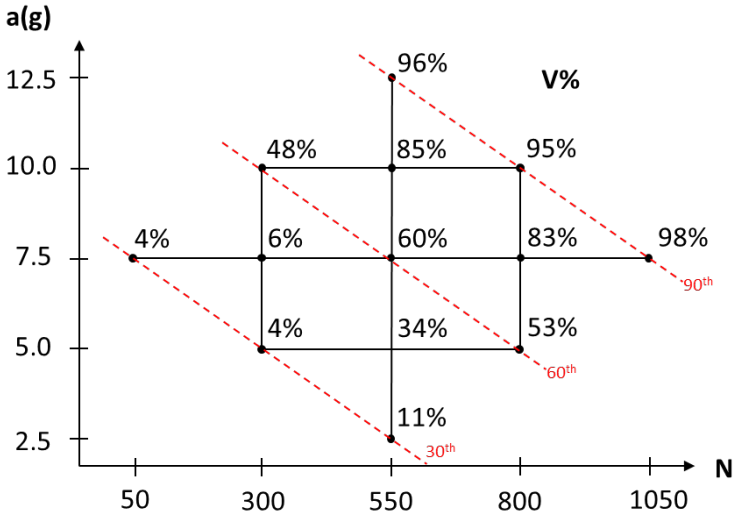


Figure 6.24: Percent Liquid Dispersion surface response grid.

The most notable difference between this grid and those for percent homogeneity and coefficient of variation is that the percent liquid dispersion has a strong nonlinear dependency on acceleration and mixing cycles. Values at the 30$^{th}$ and 60$^{th}$ percentiles, for example, are no longer similar. This nonlinearity reveals an interesting limitation to agglomerate breakup. To illustrate this limitation, I will compare agglomerate breakup along the main axes of the CCD grid. Agglomerate breakup at a constant acceleration of 7.5 g is shown in Figure 6.25. At this acceleration, percent liquid dispersion increases from just 4% at $N = 50$ to 98% at $N = 1050$. From $N = 50$ to $N = 300$, the size of the satellite drop is more or less the same with very little liquid dispersion. The only difference between these two states is the production of more daughter drops from erosion. From $N = 50$ to $N = 300$, there is a large difference in both the size and number of satellite and daughter drops.

Within this range of mixing cycles, the large agglomerate breaks into multiple fragments with volumes much less than half the agglomerate's size. This sudden jump in aggregate count is also reflected in the percent liquid dispersion as it increases from 6% to 60%. The production of more aggregates has led to an outstanding increase in liquid dispersion likely due to the increase in surface area. Following the sudden rupture of the agglomerate, the liquid dispersion continues to increase and shows signs of plateauing from $N = 550$ to $N = 1050$.

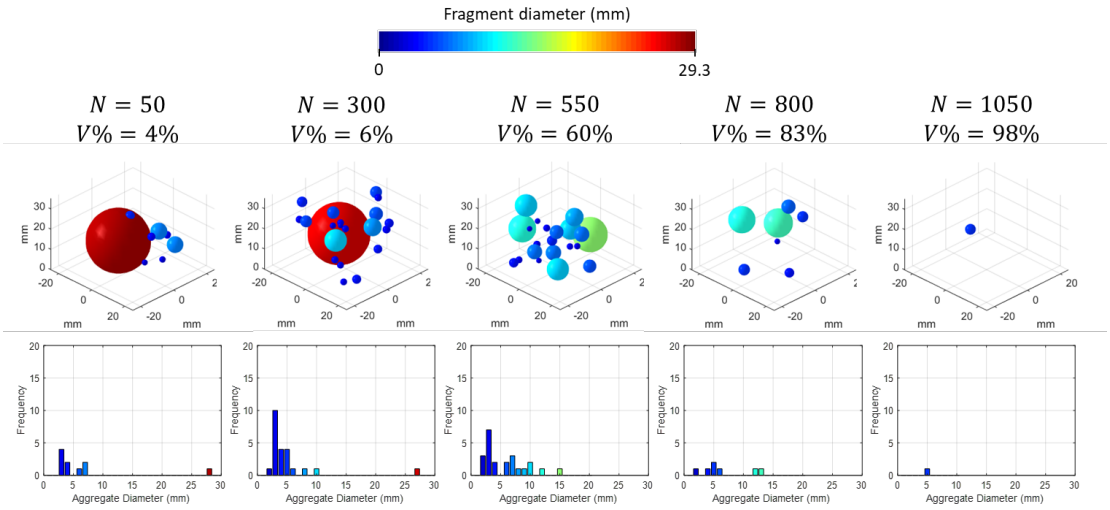


Figure 6.25: Agglomerate breakup at a constant a=7.5.

Agglomerate breakup at a constant 550 mixing cycles is shown in Figure 6.26. At this acceleration, percent liquid dispersion increases from 11% at $a = 2.5$ to 96% at $a = 12.5$. Unlike the case of constant acceleration, the agglomerates have already ruptured in all five conditions. As the number of cycles is increased, the percent liquid dispersion increases and begins to plateau at larger accelerations. From the 3D images, there is observed rupture and erosion throughout the process. This entire regime behaves much like the constant acceleration dispersion study after rupture had

occurred. Between these two studies, there is a shared point at $a = 7.5$ and $N = 550$. This condition can be reached in two ways, either through increased $a$ at constant $N$ or increased $N$ at constant $a$. Due to the realization that rupture occurs shortly prior to $N = 550$ at constant $a = 7.5$, it is desirable to get to the shared point by increasing $a$ at a constant $N = 550$.

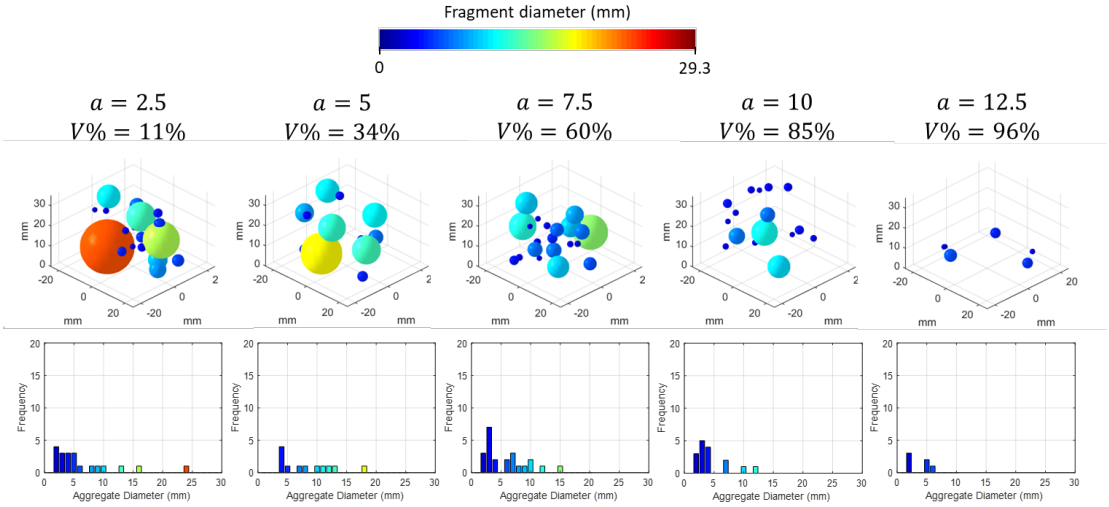


Figure 6.26: Agglomerate breakup at a constant N=550.

Investigating agglomerate breakup at constant $a$ and $N$ reveals that rupture does not occur immediately within the mixing process. The conditions for which rupture occur are still unknown, but they are related to the number of cycles. Rupture precedes the sudden jump in percent liquid dispersion and for the conditions tested it is likely to occurs below 10% liquid dispersion. This information allows us to predict the conditions for which rupture occurs.

# Chapter 7: Dispersion Modeling

In the previous chapter, investigation into the percent liquid dispersion revealed that the two modes of breakup, erosion and rupture, are present throughout the mixing processes. Erosion is observed in all combinations of $a$ and $N$, suggesting that it is an ongoing and gradual phenomenon. Rupture was also observed throughout the mixing process, though interestingly it lags erosion by a significant amount (nearly 500 cycles). As the agglomerates collide with the powder beneath and each other, force from the kinetic motion is transferred to the surface of the agglomerate. If large enough, the force may cause rupture. Otherwise, the force will contribute to erosion until the criterion for rupture is met. Though, there is still much unknown about the rupture lag and its causes. In this chapter, I will append the erosion and rupture breakup model through experimental observation of agglomerate breakup. Through experimental observation, adhesion and liquid dispersion will be observed as contributing to the physical breakup modes.

## 7.1 Appending the Breakup Model

The agglomerate breakup model of erosion and rupture is backed by the experimental data on percent liquid dispersion. Additional confirmation of the model is given by the observed breakup of the agglomerate at $a = 7.5$ shown in Figure 7.1 below. Interestingly, there is an added mode of breakup that appears through our observation: adhesion. As the mix begins, the four initial disk-shaped agglomerated immediately breach the surface and merge into a single agglomerate. The

agglomerate rising to the surface agrees with observations made by Muzzio eta al on the reverse buoyancy of a vibrating powder bed [67]–[69]. The merging of the agglomerates agrees with the agglomerate 3D images in Figure 6.23. Following the surfacing of the agglomerates, adhesion of dry particles to the merged agglomerate is observed. This is noted by the white particles on the surface of the blue agglomerate. This added mass alters the surface structure of the agglomerate, namely the porosity. Powder on the surface will draw in fluid due to capillary action, but the fluid is finite in volume. The change in fluid volume caused by the capillary action is compensated by the restricting of the surface particles, reducing their local porosity. Adhesion is then proceeded by erosion. With the arrival of adhesion, erosion is now facilitated through two operations. Erosion is still caused by the collision of the agglomerate with the dry powder but is now made easier due to the decrease in porosity. The porosity defines the void volume, and for a given particle size a change in porosity causes a change in capillary radius. The lower local capillary pressure requires less stress to overcome, therefore erosion is increased due to adhesion. Adhesion and erosion will continue until rupture is present, though there is one major difference between the wet-dry system initial and on the onset of rupture and that is the dry powder itself.

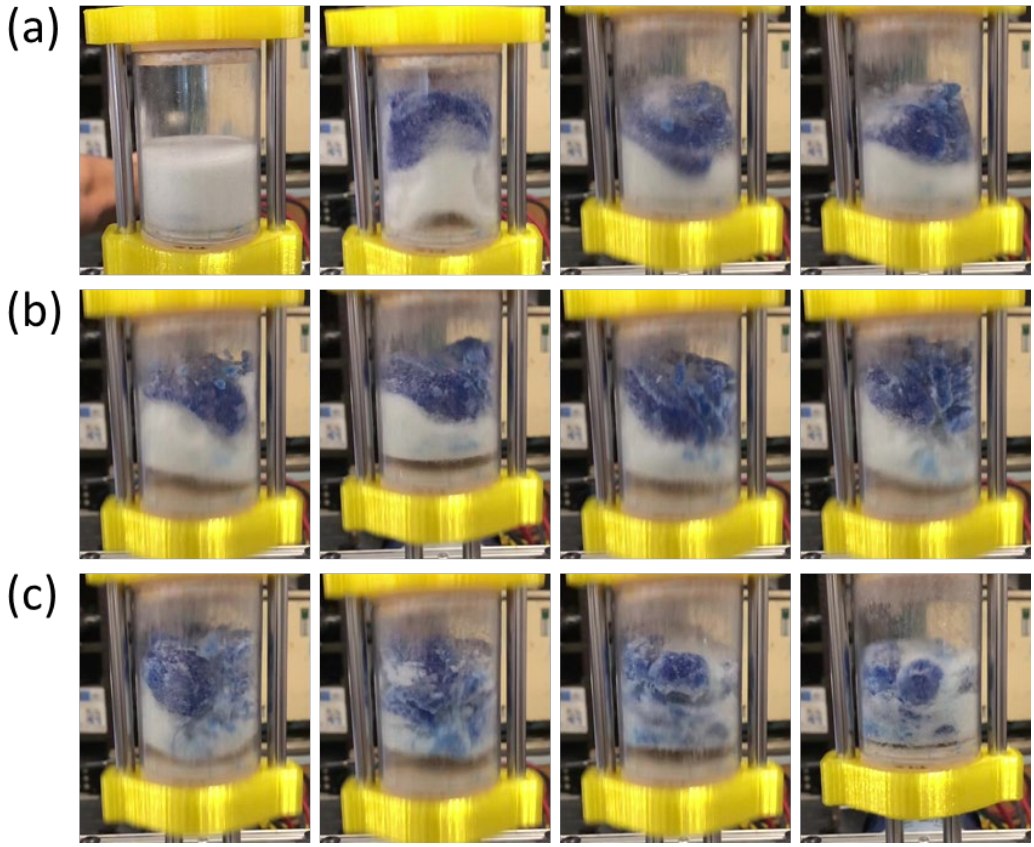


Figure 7.1: Observed agglomerate breakup at a=7.5. (a) adhesion and erosion observed, (b) liquid dispersion observed, and (c) onset of rupture.

Initially, the powder surrounding the agglomerate is unsaturated. Oscillations of the mixing platform vibrate the dry powder bed and launch the dry powder as it does the agglomerate. The unsaturated powder flows freely, much like a fluid [17], [70], [71]. Near the onset of rupture, the unsaturated powder behaves much differently. It is no longer fluidized and sticks to itself mostly. The reasoning behind this change is the dispersion of the fluid. Liquid dispersion was found to increase as mixing time increased. Before rupture occurs, fragments of the agglomerate that have broken off due to erosion become embedded in the dry powder. Once embedded, the liquid trapped inside the fragment wicks the surrounding powder, partially saturating

it. As mixing continues, the amount of liquid dispersed by this method increases resulting in a more saturated porous matrix. Rupture is observed once the surrounding powder is partially saturated, at which the force transfer between the powder matrix and the agglomerate is sufficient to break the agglomerate into large fragments. This suggests that the initial dry powder dissipates the mixing forces produced by the vibrations and explains why rupture does not occur immediately. As the dry powder carries more fluid, however, it dissipates less energy, therefore more energy can be put into rupture. These two additional breakup modes are illustrated in Figure 7.2 and are used to explain the conditions for breakup in a vertically vibrating powder system.

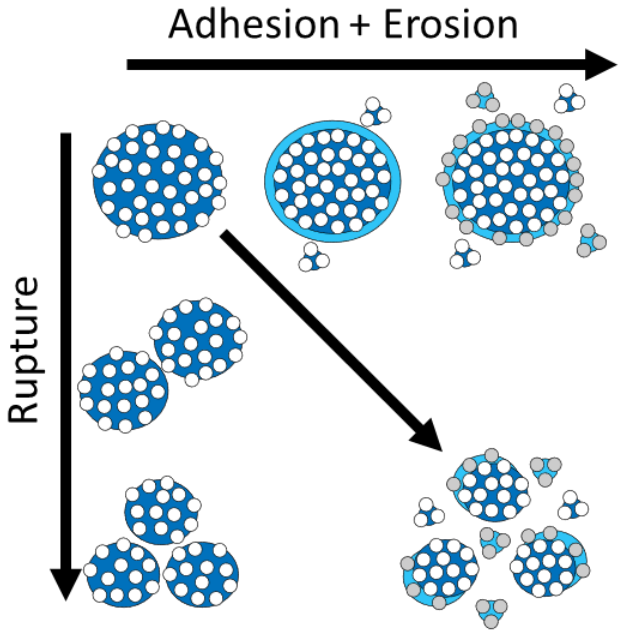


Figure 7.2: Fracture model incorporating adhesion to the traditional dispersion model of erosion and rupture.

# Chapter 8: Conclusions

The effect of initial charging of a vertically reciprocating mixer on mix quality was evaluated through study of feed protocol and operating conditions. For our material system, we have been able to achieve excellent homogeneity (%H > 93%) as a function of acceleration and cycles. Using DOE-CCD we have generated predictive equations for percent homogeneity (%H), coefficient of variation (Cv), and liquid dispersion (V%).

The most important factor for the breakup of agglomerates is the impact with the ends. Removal of the dry solids, which can act as force dissipaters, is achieved primarily by adhesion to the wetted agglomerates, which we have identified as a critical mechanism. We have found that once a sufficient number of solids have be adsorbed, there would be a rapid breakup of the agglomerates to smaller sizes.

A theoretical model for fluid flow within a powder, the Washburn equation, was used to determine the effect of fluid properties on size and shape of the wetted region formed through initial charging. Increasing the fluid viscosity, for instance, can impede the wicking rate of a fluid. Through static experimentation, the shape of the wetted region could be predicted given the particle size, fluid properties, and feed rate. The static experiment revealed a wicking rate that is dependent on both feed rate and powder composition. At sufficiently high feed rates, the critical wicking rate no longer varies with powder composition. This suggests that the feed rate is much higher than the critical wicking rate of any powder composition. The critical wicking

rate is used to augment the shape of the initial agglomerate. Using liquid feed rates under the critical rate will result in more wicking and liquid feed rates above the critical value will result in more wetting. This surface spreading information is used to determine a dispensing array to maximize the amount of powder wetted prior to mixing.

In the dynamic experiment, the number of cycles, $N$, was chosen over time due to cyclic nature of the force transfer between ingredients. With the range of accelerations and number of cycles tested, the quality of the mixture ranged from 30% mixed to 90% mixed. Central composite design revealed a first order dependency of mix quality to acceleration, $a$, and number of cycles, $N$ with a $p_{value} < 0.001$. The empirical relationship shows the significance each of the mixing parameters has on the quality of the mixture. Three-dimensional views of the samples are used to gage the degree of breakup of the initial agglomerates. Satellite drop size was found to be inversely proportional to the quality of the mixture, with the largest satellite drops populating samples of the 30th percentile. Erosion was found to be present in all mixing conditions, with eroded daughter drops having a common diameter size of 3 mm. Rupture, on the other hand, did not occur until a sufficient number of mixing cycles were completed. Through experimental observation, this behavior was attributed to the dissipative nature of fluidized powder [72]–[74]. The force dissipated by the surrounding powder depends on the amount of liquid dispersed into the powder. As more liquid is dispersed, fewer mixing forces are dissipated and therefore rupture may proceed. Adhesion of dry particles to the wet agglomerate was also found to affect breakup by reducing the local capillary pressure.

These two additional aspects alter the traditional erosion and rupture breakup model for vertically vibrating mixers.

## 8.1 Future Research

The work presented here details agglomerate breakup within a vertically vibrating mixer for a single liquid and solid pairing. To improve the generality of the breakup model, future research will investigate the effect of material selection on final product variation, rather than through optimization of mixing parameters. In this research, the variables that may affect blend homogeneity are unique to both liquid and solid phases. For the liquid phase, the main variable is viscosity, which appears in the Lucas-Washburn equation and is inversely correlated with wicking depth. For the solid phase, the main variable is particle size. In a unimodal system, the pore size is proportional to particle size with smaller-sized particles yielding smaller pores and in turn, smaller capillary radii. The capillary radius significantly affects both static and dynamic diffusion. In static diffusion, the capillary radius appears in the Lucas-Washburn equation and is proportional to wicking depth. At smaller particle sizes, the wicking depth will decrease. In dynamic diffusion, the capillary radius appears in the capillary pressure equation and is inversely proportional to the pressure. For smaller particles, this means that the pressure holding agglomerates together is greater and requires more force to overcome. An additional variable worth investigating is the container fill. In our study, the initial loading of ingredients filled 66% of the container volume. The reasoning behind this value was to eliminate agglomerate collisions with the roof of the container, therefore limiting collisions to once per cycle. As the fill of the container increases, collisions between the agglomerate and

the container roof will be more frequent and may improve breakup rates. However, increasing fill can also limit the diffusion of eroded particles into the powder bed and lead to a larger lag in rupture.

The effect of these three variables on blend homogeneity can be evaluated in a similar manner to the work presented earlier and using a 5 degree-of-freedom surface response design. Acceleration and number of cycles will remain within the range of 2.5-12.5 g and 50-1050 cycles respectively. Particle size will vary between 100 and 300 μm. Viscosity will range between 200 and 1000 cSt. Finally, container fill will vary within the range of 50-100% full. Through evaluation of these additional variables, it will be possible to determine fully generalizable optimizations to reduce blend variation and deduce a fully generalizable breakup model for agglomerates under vertical vibration.

# Appendices

## Appendix A: Mixing Measure Error

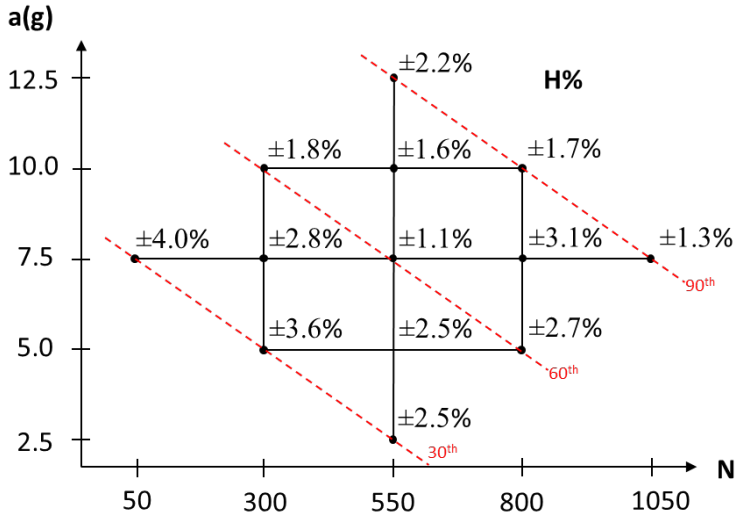


Figure A.1: Percent homogeneity standard deviation error for four repeated experiments.

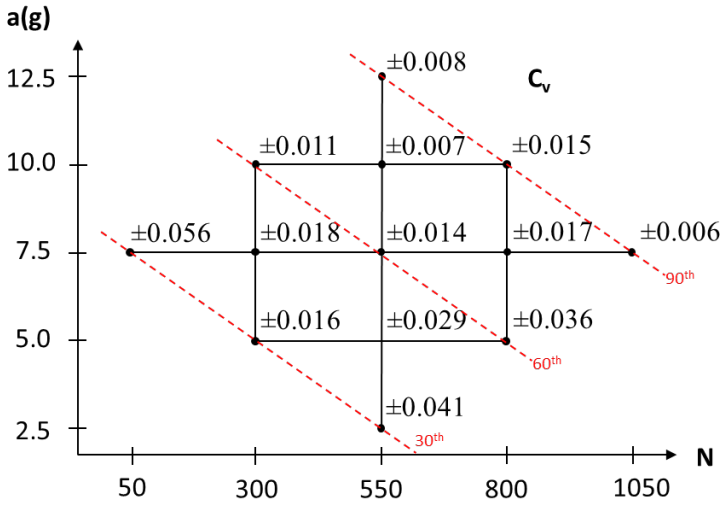


Figure A.2: Coefficient of variation standard deviation error for four repeated experiments.

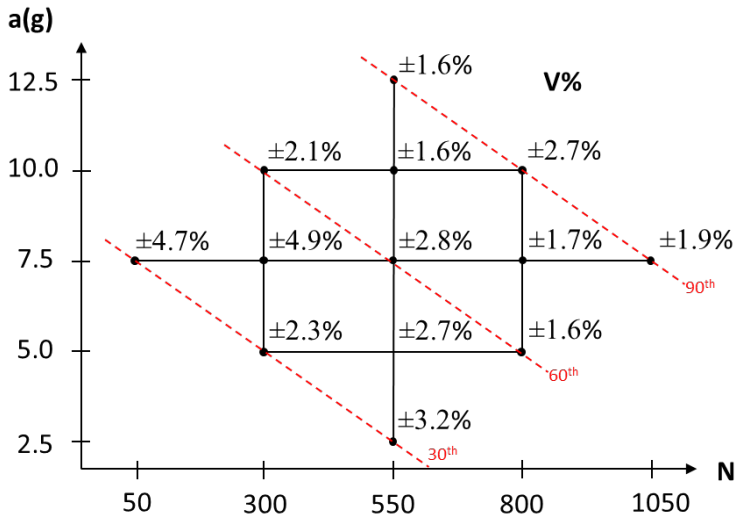


Figure A.3: Percent liquid dispersion standard deviation error for four repeated experiments.

## Appendix B: Mixing Apparatus Harmonic Response

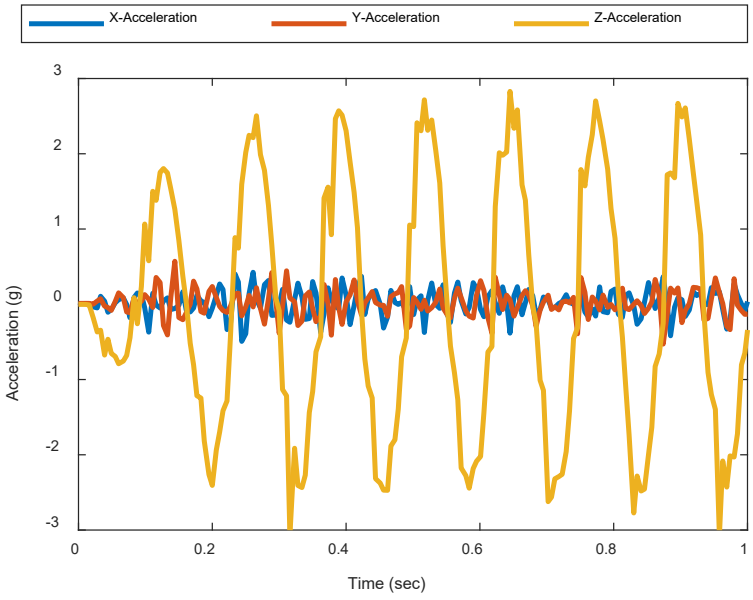


Figure A.4: Mixing apparatus harmonic response at 2.5 g

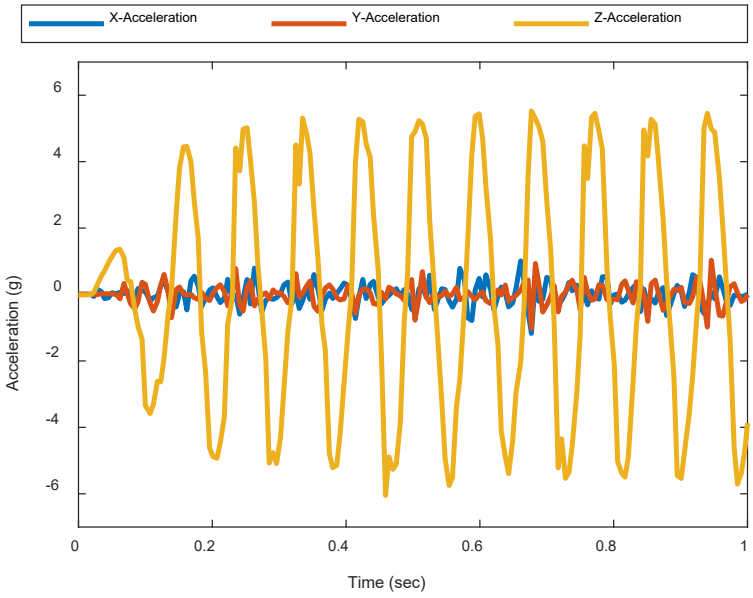


Figure A.5: Mixing apparatus harmonic response at 5 g

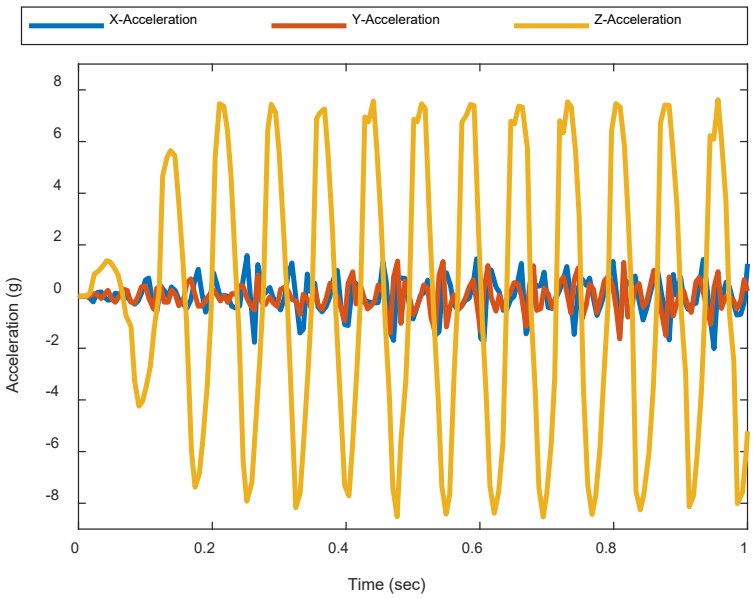


Figure A.6: Mixing apparatus harmonic response at 7.5 g

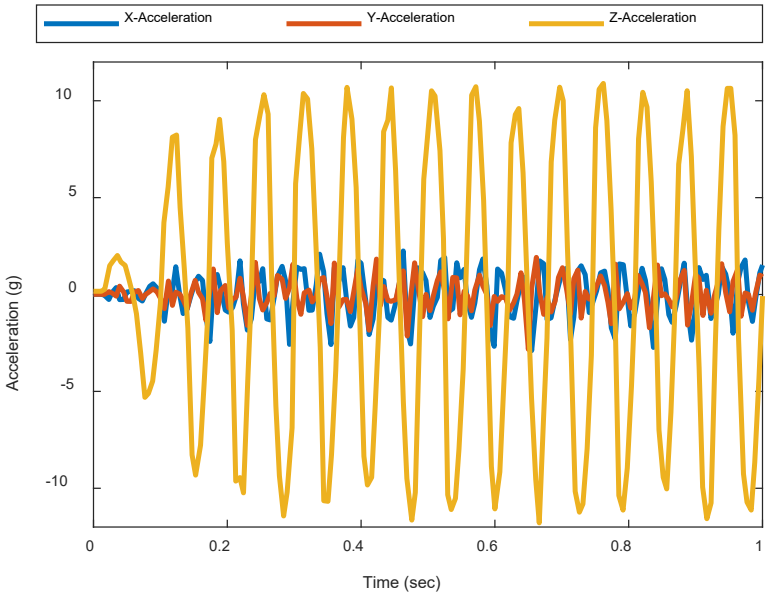


Figure A.7: Mixing apparatus harmonic response at 10 g

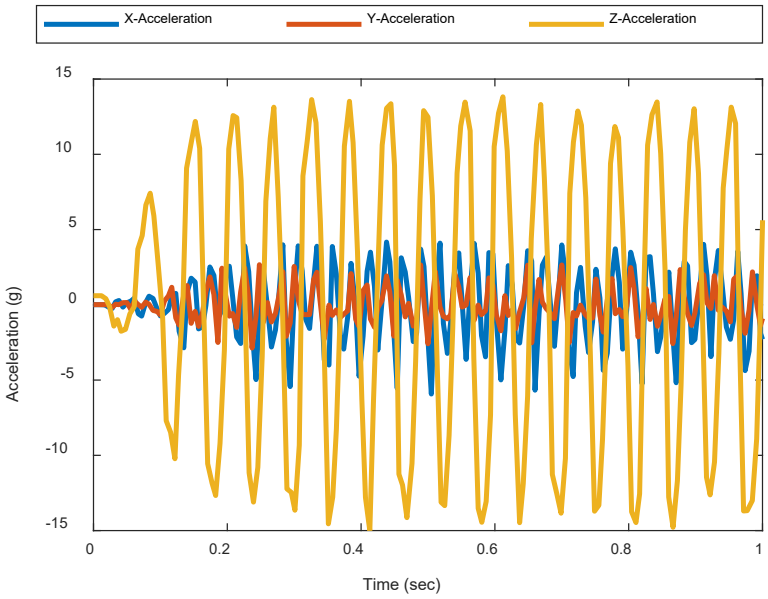


Figure A.8: Mixing apparatus harmonic response at 12.5 g

## Appendix C: Mixing Apparatus Technical Drawings

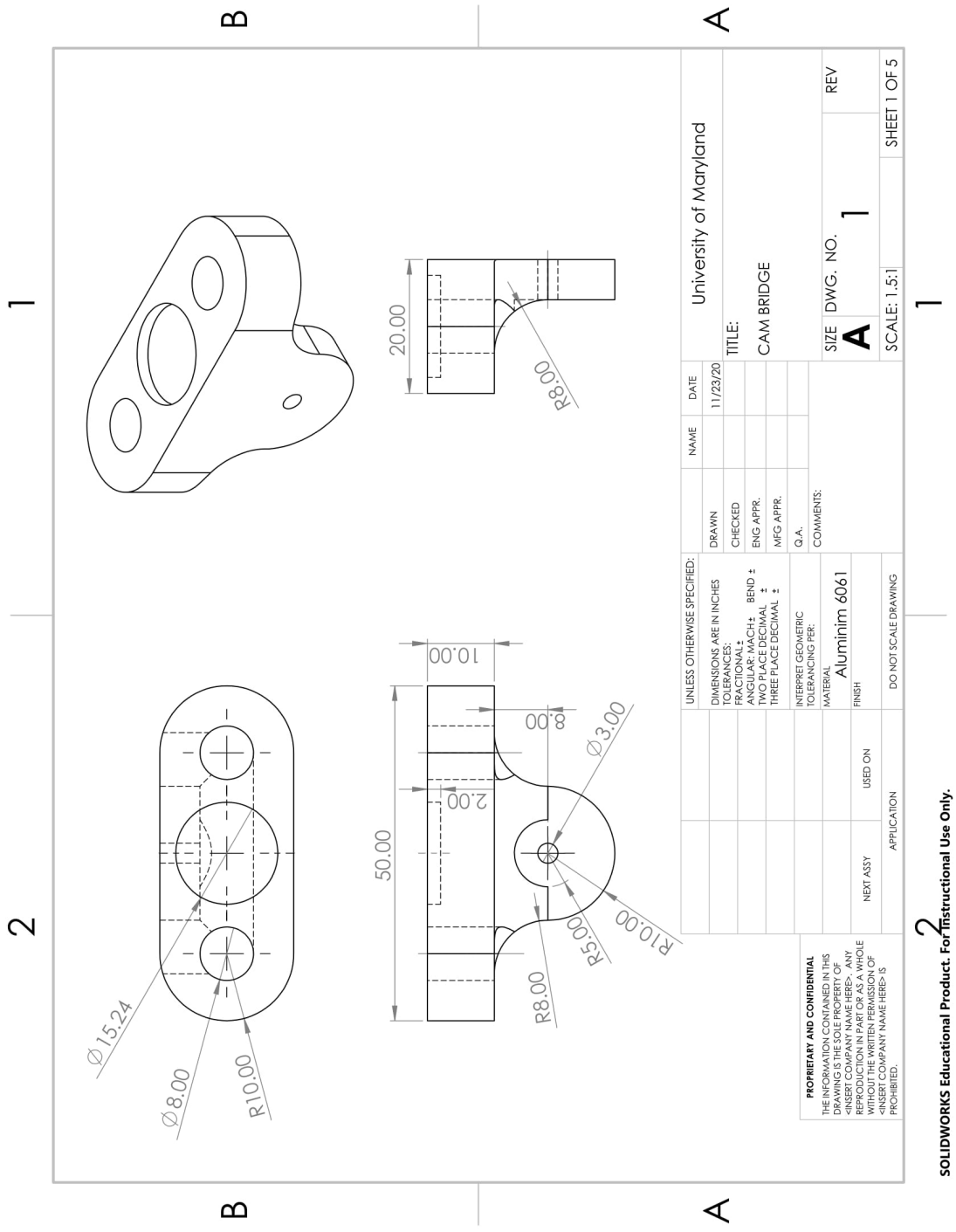


Figure A.9: Cam bridge technical drawing

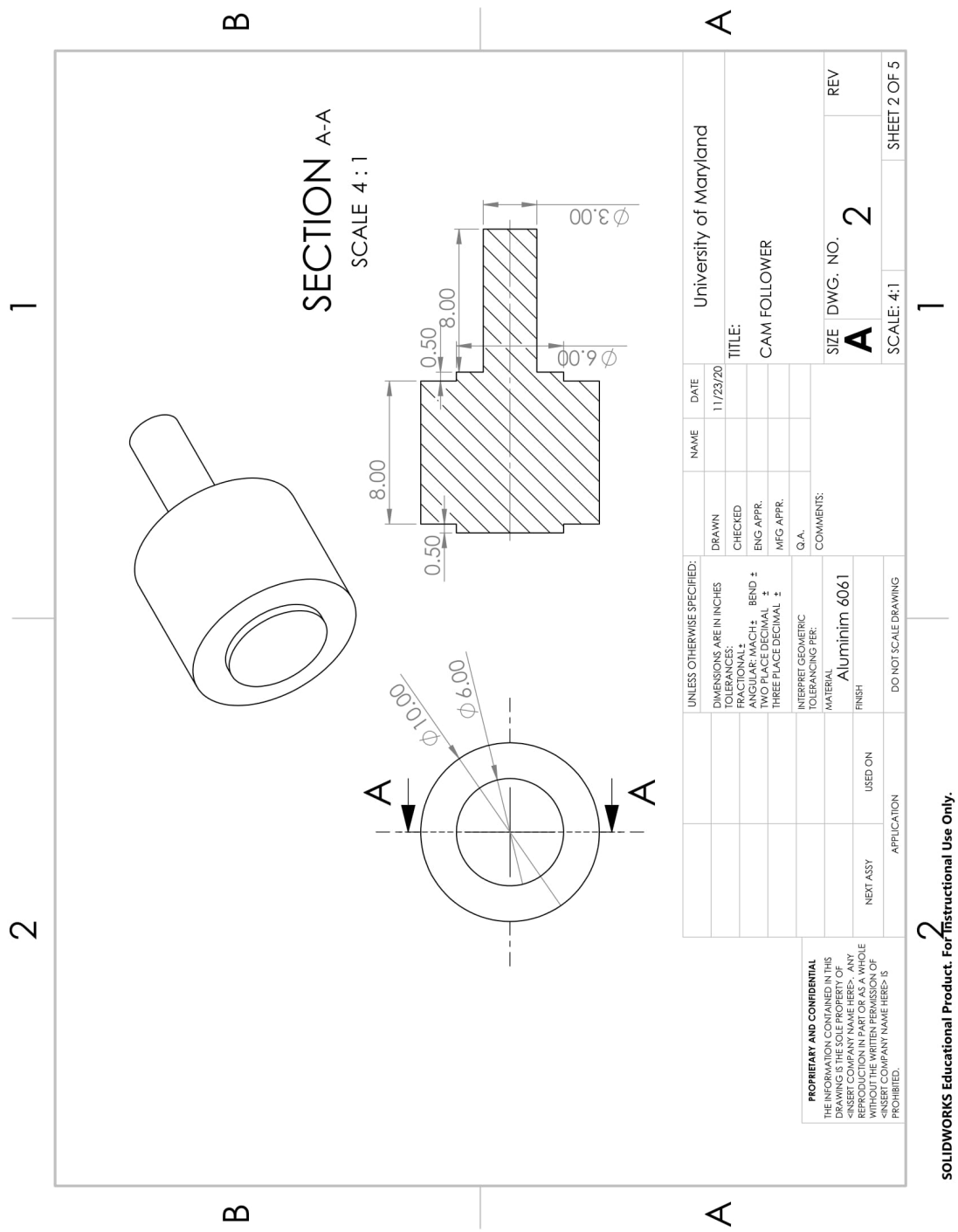


Figure A.10: Cam follower technical drawing

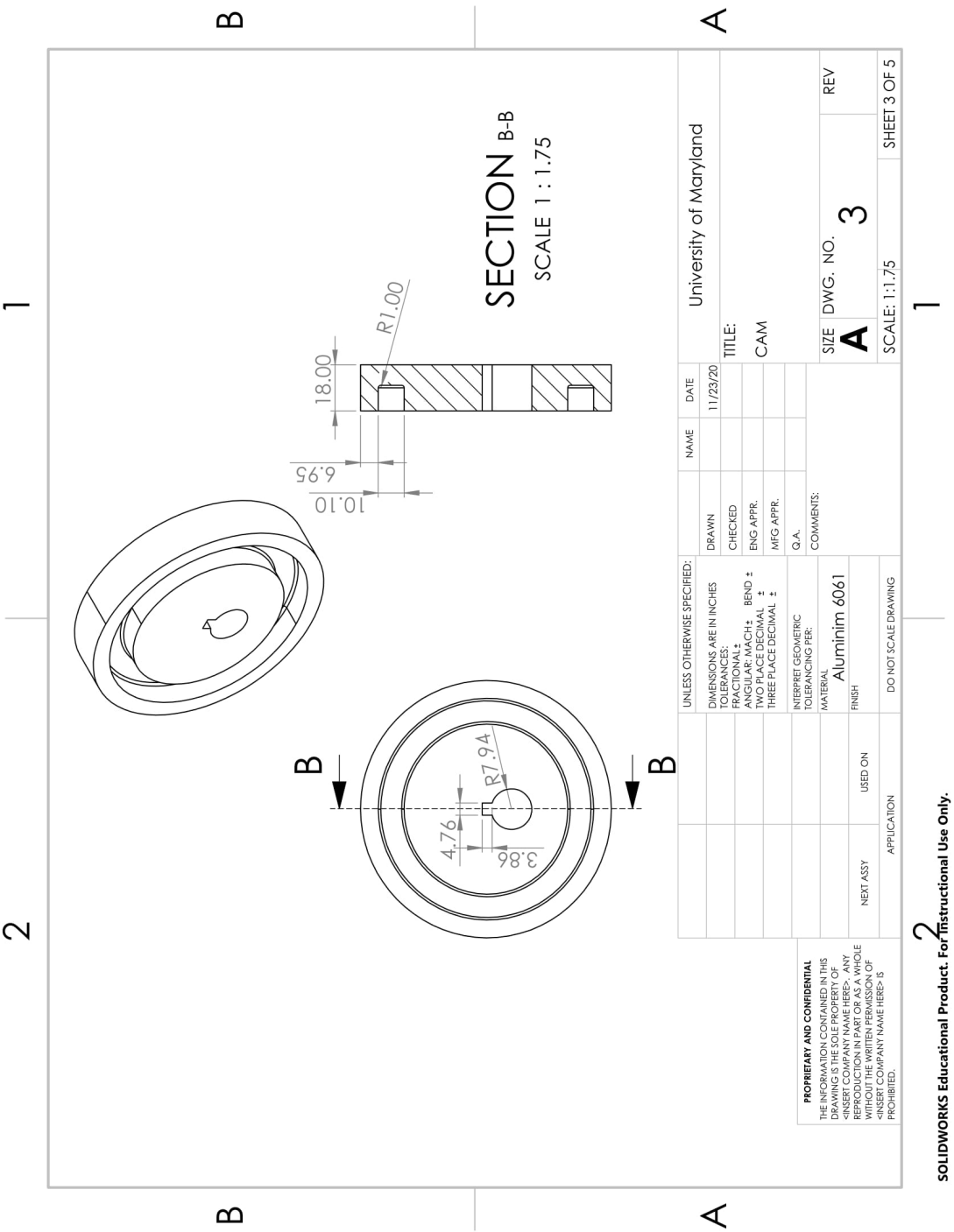


Figure A.11: Cam technical drawing

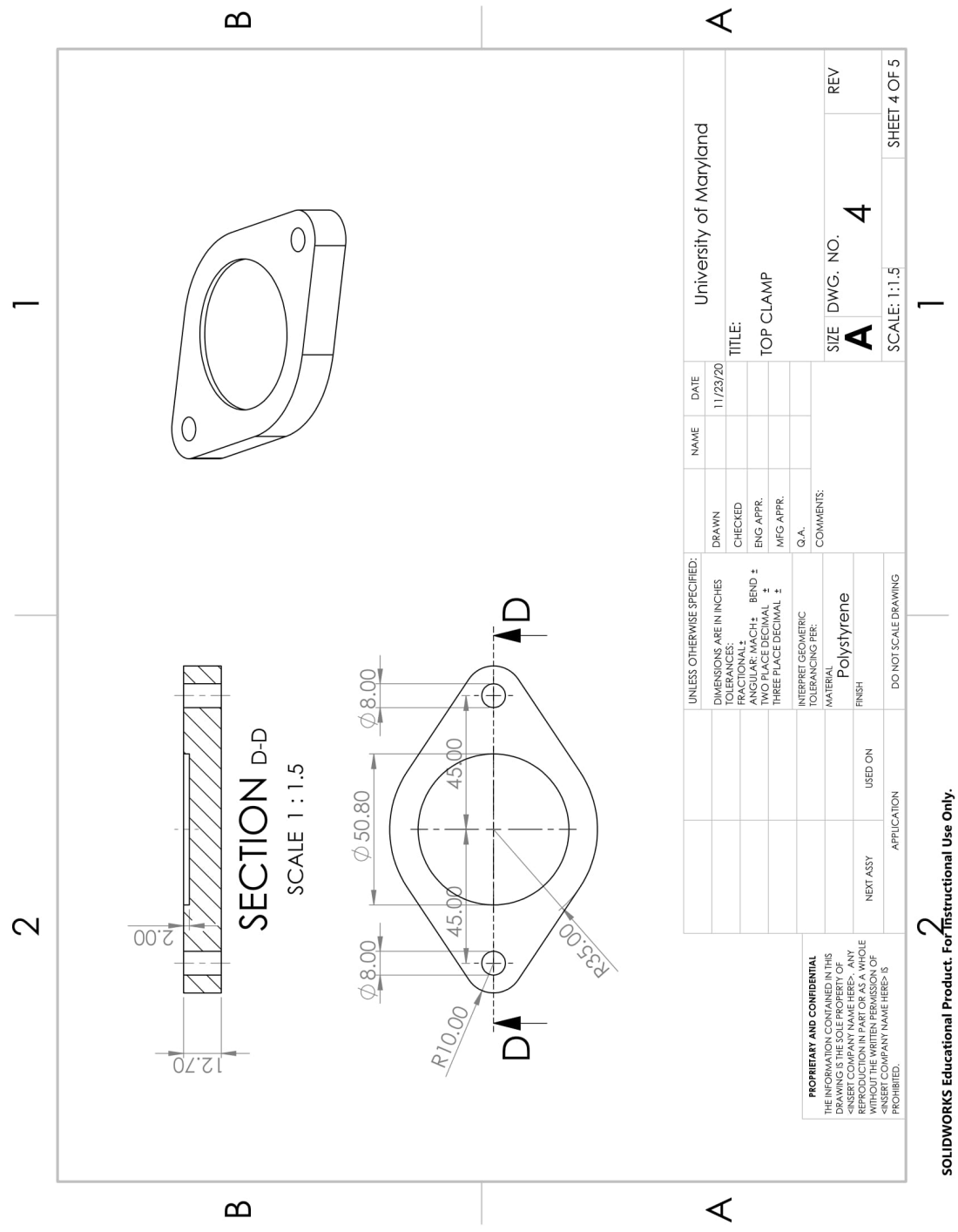


Figure A.12: Top container clamp technical drawing

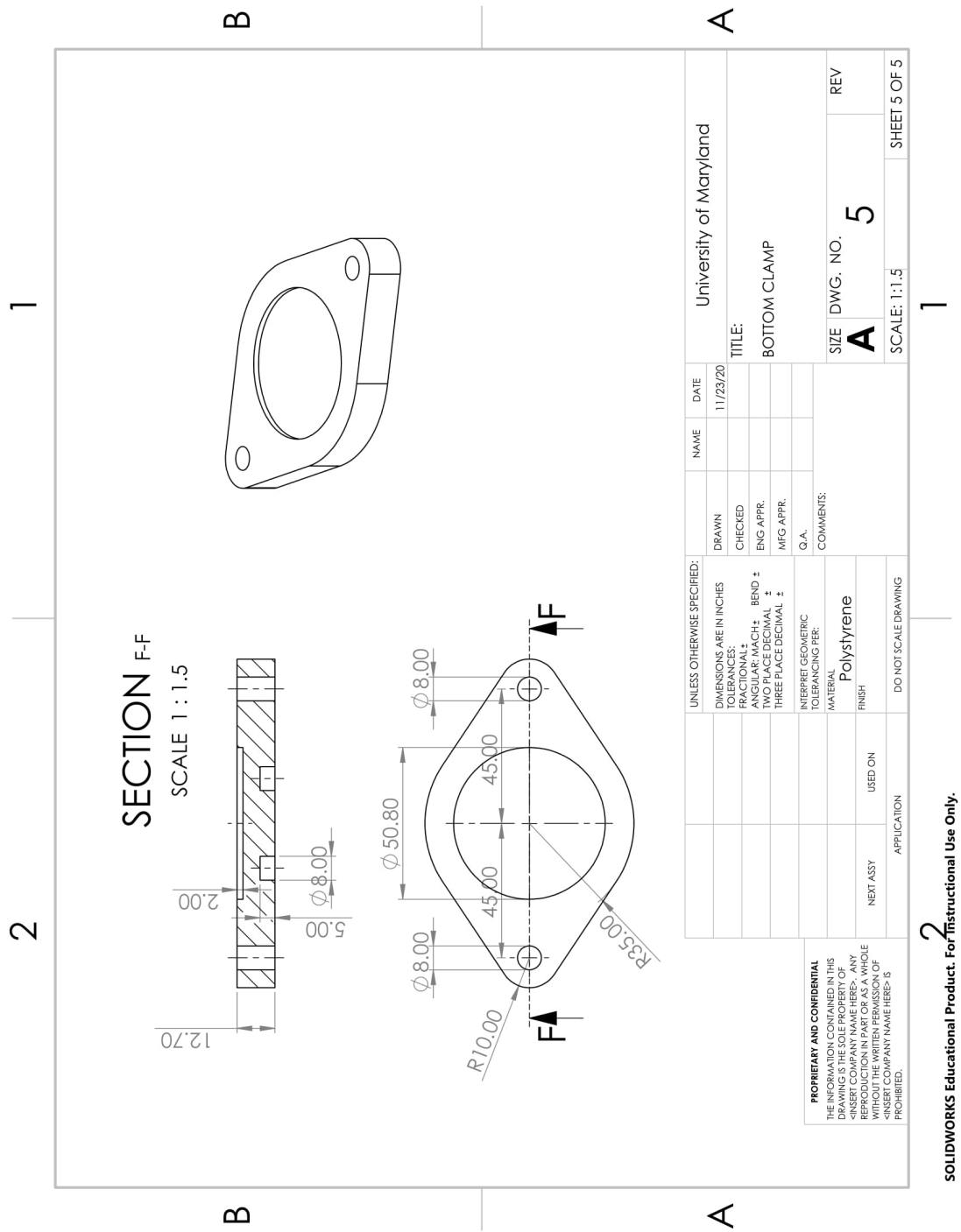


Figure A.13: Bottom container clamp technical drawing

# Appendix D: Image Processing Algorithms

## D.1 Wetting Diameter

```
close all;
clear all;
clc;

% Experiment information
trial_num = 5;
experiment = 'Trial 2';
threshold = 15;
ref_width = 74.5; %63 mm for a 250 mL beaker

vid = VideoReader('Trial 2 Diameter.mp4');
n = vid.NumberOfFrames;
fps = vid.FrameRate;

frame_width = size(image, 2);

Transcient_Area = [];
Transcient_Aspect = [];
Transcient_Center = [];
Transcient_Box = [];

temp1 = read(vid,1);
figure(1);
[temp1 width_crop] = imcrop(temp1);
conversion_factor = ref_width/width_crop(3);

temp = read(vid,n-1);
figure(1);
[temp rect_crop_whole] = imcrop(temp);
rect_crop_whole=round(rect_crop_whole/2)*2;
crop_x=rect_crop_whole(1);
crop_y=rect_crop_whole(2);
crop_width=rect_crop_whole(3);
crop_height=rect_crop_whole(4);

background = read(vid,1);
frame_height = size(background, 1);
frame_width = size(background, 2);
blank = zeros(frame_height, frame_width);

background = rgb2gray(background);
background = imcrop(background,rect_crop_whole);

Image_conversion_factor = [];
Width_mm = [];
Length_mm = [];
Diameter_mm = [];
x = [];
time = [];

processed_vid=strcat(experiment,' Processed.mp4');
new_vid = VideoWriter(processed_vid,'MPEG-4');
```

1

```
new_vid.FrameRate = fps;
open(new_vid);

for j = 2:n   % Loops through the entire number of frames between the
 time intervals
    frame = read(vid,j);
    file = rgb2gray(frame);
    file = imcrop(file,rect_crop_whole);

    new=imabsdiff(background,file);

    startrow = crop_y;
    startcol = crop_x;
    blank(startrow:startrow+size(new,1)-1,startcol:startcol
+size(new,2)-1) = new;

    newI = mat2gray(blank);
    newI = imbinarize(newI,threshold/double(max(max(new))));
    newI = medfilt2(newI,[4 4]);
    newI = imfill(newI,'holes');

    %figure(1);
    %imshow(newI);             % Shows resulting image

    shapes = bwconncomp(newI, 4);   % Finds connected components in
 the image
    data =
 regionprops(shapes, 'Area', 'Centroid', 'BoundingBox', 'Eccentricity');
   % Measures properties of connected components
    ecc = [data.Eccentricity];
    area = [data.Area];
    center = [data.Centroid];
    box = [data.BoundingBox];
    aspect_ratio = (1-ecc.^2).^(-0.5);

    % The following block of code gathers the pixel data and
    % converts/places it into a set of arrays
    [M,nn] = max(area);
    area = area(nn);
    aspect_ratio = aspect_ratio(nn);
    center = [center(2*nn-1), center(2*nn)];
    box = [box(4*nn-3), box(4*nn-2), box(4*nn-1), box(4*nn)];

    processed_image = false(size(newI));
    processed_image(shapes.PixelIdxList{nn}) = true;
    writeVideo(new_vid,im2single(processed_image));

    Transcient_Area = [Transcient_Area; area];
    Transcient_Aspect = [Transcient_Aspect; aspect_ratio];
    Transcient_Center = [Transcient_Center; center];
    Transcient_Box = [Transcient_Box; box];

    Image_conversion_factor = [Image_conversion_factor;
 conversion_factor];
```

```
    Width_mm = [Width_mm; box(3)*conversion_factor];
    Length_mm = [Length_mm; box(4)*conversion_factor];
    Diameter_mm = [Diameter_mm; sqrt(area*(4/pi))*conversion_factor];
    time = [time; j/fps];

    round(100*(j/n))
end
close(new_vid);
x = [x; [1:n-1]'];
length(x);
length(Transcient_Area);

Total_Data = [x, Transcient_Area, Transcient_Aspect,
 Image_conversion_factor,...
    Diameter_mm, time];
Total_Data = ["IMG", "Area (px^2)", "Aspect Ratio", "Resolution (mm/
px)",...
    "Diameter (mm)", "Time (s)"; Total_Data];

% Creates the excel file containing all of the data
xlswrite(strcat(experiment,' Data.xlsx'), Total_Data);


ans =

     1


ans =

     2


ans =

     2


ans =

     3


ans =

     3


ans =

     4


ans =
```

```
ans =

    99

ans =

    99

ans =

   100
```

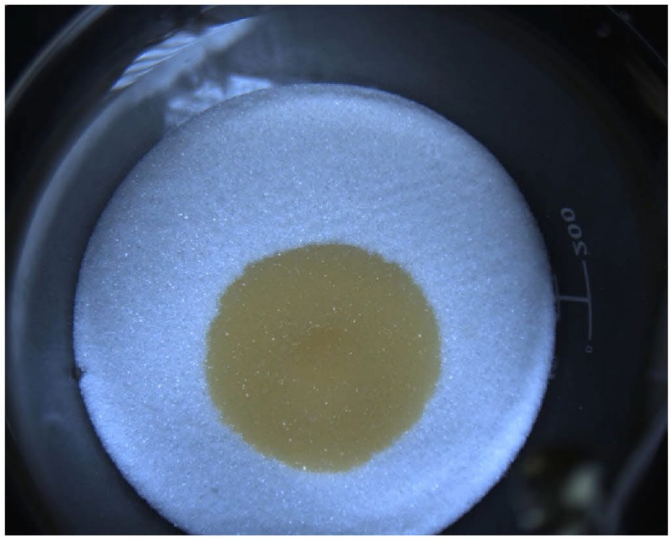

*Published with MATLAB® R2019a*

```
%close all;
clear all;
```

# Initialization

```
folder = 'EXP89-102120-4Lkk';
ns = 550;
acc = 5;

d = 47.7; % diameter in mm
rect = [189.51 47.51 890.98 882.98];
pxs = [1024 1280];

imagefiles = dir([folder,'/*.jpg']);
nfiles = length(imagefiles);    % Number of files found
Homogeneity = [];
Variance = [];
Ls = 5:-0.5:0.5;
Ls = 2;
iis = 0;

for L = Ls
    N = 0;
    AAA = [];
    Percent_Homogeneity = [];
    VVV = [];
    disp([num2str(iis),'/',num2str(length(Ls)),' done']);
    iis = iis+1;

    % Loop to create squares
    for ii = 1:nfiles
        currentfilename = imagefiles(ii).name;
        currentimage = imread([folder,'/',currentfilename]);
        I = currentimage;
        I = rgb2gray(I);
%         if ii == 1
%             figure(1); clf;
%             imshow(I);
%             figure(2); clf;
%             imhist(I);
%         end

        %[I2, rect] = imcrop(I);
        res = d/rect(3); % mm/px ratio
        r_px = round(min(rect(3),rect(4))/2); %radius of container in
 px
        L_px = round(L/res); % length of bin in px
        center = [rect(1)+rect(3)/2 rect(2)+rect(4)/2];
        center = round(center);

        r_px_r = L_px*floor(r_px/L_px); %rounded length of container
 in px
```

```
        if ii == 1
            rects = [];
            for i = 1:2*r_px_r/L_px
                for j = 1:2*r_px_r/L_px
                    rect_tmp = [-r_px_r+L_px*(i-1) -r_px_r+L_px*(j-1)
L_px L_px];
                    pts = [rect_tmp(1) rect_tmp(2);...
                        rect_tmp(1)+rect_tmp(3) rect_tmp(2);...
                        rect_tmp(1) rect_tmp(2)+rect_tmp(4);...
                        rect_tmp(1)+rect_tmp(3)
rect_tmp(2)+rect_tmp(4)];
                    dist = sum(pts.^2,2);
                    if sum(dist<r_px^2*ones(4,1)) == 4
                        rects = [rects; rect_tmp];
                    end
                end
            end
            rects(:,1:2) = rects(:,1:2)+center;
            rects_size = size(rects);
            n = rects_size(1); % number of squares per slice
        end

        N = N+n; % total number of squares
        sub_s = imcrop(I,rects(1,:));
        [h,w] = size(sub_s);
        h = h-1;
        w = w-1;

        for i = 1:n
            sub_s = imcrop(I,rects(i,:));
            sub_s(end,:) = [];
            sub_s(:,end) = [];
            A = reshape(sub_s,w*h,1);
            AAA = [AAA; A];
        end
    end

    % Global Mixing Index
    BBB = randsample(AAA,N*w*h);
    X = [];
    STD = [];
    X_r = [];
    STD_r = [];

    for i = 1:N
        AAAA = AAA(1+(i-1)*h*w:i*h*w);
        BBBB = BBB(1+(i-1)*h*w:i*h*w);
        sub_r = reshape(BBBB,h,w);
        sub_s = reshape(AAAA,h,w);

        X = [X mean2(sub_s)]; % Means of macropixels of image
        X_r = [X_r mean2(sub_r)]; % Means of macropixels of randomized
image
```

```
        STD = [STD std2(sub_s)]; % STD of macropixels of image
        STD_r = [STD_r std2(sub_r)]; % STD of macropixels of
 randomized image
    end

    ll = N/nfiles;

    M_t = mean(X); % Avg of macropixel means
    M_t_r = mean(X_r); % Avg of randomized macropixel means
    std_m = sqrt(sum((X-M_t).^2)/N); % Std of macropixel means
    std_m_r = sqrt(sum((X_r-M_t_r).^2)/N); % Std of randomized
 macropixel means

    M_sd = mean(STD); % Avg of std of macropixels
    M_sd_r = mean(STD_r); % Avg of std of randomized macropixels

    H2 = (M_sd/M_sd_r);
    VAR = std_m/M_t_r;


    Homogeneity = [Homogeneity H2];
    Variance = [Variance VAR];
end
```

```
0/1 done
```

# Measures of Mixing Values

```
Homogeneity
Variance

%I = std_m^2/M_t % Intensity of Segregation
B = sum((X-M_t).^2)/(N*M_t) % Scale of Segregation
```

```
Homogeneity =

    0.9502


Variance =

    0.0531


B =

    0.1855
```

*Published with MATLAB® R2019a*

## D.3 Liquid Dispersion and 3D Imaging

### Table of Contents



```
clear all;
clc;
```

# Initialization

```
folder = 'EXP28-042820-4Lkk'; % Experiment name
acc = 7.5; % acceleration in g's
cyc = 800; %  number of mixing cycles
imagefiles = dir([folder,'/*.png']);
nfiles = length(imagefiles);    % Number of files found
sc = 0.8;

d = 47.7; % container diameter in mm
rect = [189.51 47.51 890.98 882.98];
thickness = 2; % slice thickness in mm
center = [rect(1)+rect(3)/2 rect(2)+rect(4)/2];
center = round(center);

total_area = [];
total_centers = [];
total_box = [];
total_aspect_ratio = [];
total_diameters = [];

hist_diameters = [];
mat_3D = [];
V_init = 3299; % volume of initial disk in mm^3
```

# Loop to generate 3D matrix

```
for ii=1:nfiles
    currentfilename = imagefiles(ii).name;
    currentimage = imread([folder,'/',currentfilename]);

    I = currentimage;
    %I = rgb2gray(I);
    Ibw = imbinarize(I);
    Ibw = Ibw(:,:,1);
%     figure(2); clf;
%     imshow(I)
```

```
    %Ibw = imbinarize(rgb2gray(I));
    Ibw = imfill(Ibw,'holes');
    res_xy = d/rect(3); % mm/px ratio
    res_z = thickness;

    shapes = bwconncomp(Ibw, 4);                    % Finds connected
 components in the image
    data = regionprops(shapes, 'Area', 'Centroid', 'BoundingBox');   %
 Measures properties of connected components
    %ecc = [data.Eccentricity];
    area = [data.Area];
    centers = [data.Centroid];
    box = [data.BoundingBox];
    %aspect_ratio = (1-ecc.^2).^(-0.5);
    diat = 1/res_xy;
    areat = pi*diat^2/4;
    if max(area)>areat
        Ibw2 = bwareafilt(Ibw, [areat max(area)]);
    else
        Ibw2 = bwareafilt(Ibw, [areat areat+1]);
    end

    mat_3D(:,:,ii) = Ibw2;
    disp([num2str(ii),'/',num2str(nfiles),' done']);
end
```

```
1/14 done
2/14 done
3/14 done
4/14 done
5/14 done
6/14 done
7/14 done
8/14 done
9/14 done
10/14 done
11/14 done
12/14 done
13/14 done
14/14 done
```

# Generate 3D binary image

```
shapes_3D = bwconncomp(mat_3D,6);
data_3D =
 regionprops3(shapes_3D, 'Volume', 'Centroid', 'BoundingBox', 'ConvexHull', 'Conve
volume = [data_3D.Volume];
centers_3D = [data_3D.Centroid];
box_3D = [data_3D.BoundingBox];
ch = data_3D.ConvexHull;

volume = volume*res_xy*res_xy*res_z;
diameters = 2*(volume*(3/4)/pi).^(1/3);
```

```
radii = diameters/2;

centers_3D(:,1) = (centers_3D(:,1)-center(1))*res_xy;
centers_3D(:,2) = (centers_3D(:,2)-center(2))*res_xy;
centers_3D(:,3) = centers_3D(:,3)*res_z;

% figure(1); clf;
% h = isosurface(mat_3D);
% h.FaceLighting = 'gouraud';
% h.AmbientStrength = 0.8;
% h.DiffuseStrength = 0.5;
% h.SpecularStrength = 0.3;
% h.SpecularExponent = 25;
% h.BackFaceLighting = 'unlit';
```

# Plot spheres

```
d_max = 2*(4*V_init*3/(4*pi))^(1/3);
%df = floor((volume/(4*V_init))*63)+1;
df = floor((diameters/d_max)*63)+1;
p = colormap(jet);
col = zeros(length(diameters),3);
for k=1:length(diameters)
  a=df(k);
  col(k,:)=p(a,:);
end

[X,Y,Z] = sphere;
figure(2); clf;
for ii = 1:length(diameters)
    h =
 surf(X*radii(ii)+centers_3D(ii,1),Y*radii(ii)+centers_3D(ii,2),...

 Z*radii(ii)+centers_3D(ii,3),'FaceColor',col(ii,:),'EdgeColor','none');
    hold on;
    %h.FaceColor = 'blue';
    h.FaceLighting = 'gouraud';
    h.AmbientStrength = 0.8;
    h.DiffuseStrength = 0.5;
    h.SpecularStrength = 0.3;
    h.SpecularExponent = 25;
    h.BackFaceLighting = 'unlit';
end
%camlight left; lighting phong
%R=[rect(3)*res_xy/2 rect(3)*res_xy/2];
%N=100;
%[X,Y,Z] = cylinder(R,N);
%testsubject = surf(X,Y,Z*max(centers_3D(:,3)));
%set(testsubject,'FaceAlpha',0.5)
axis equal;
axis([-25 25 -25 25 0 35]);
view(45,30);
set(gcf, 'Units', 'Inches', 'Position', [3, 3, 4*sc, 3*sc]);
```

```
%shading interp
lightangle(-45,30)
% % h.FaceLighting = 'flat';
% h.AmbientStrength = 0.1;
% h.DiffuseStrength = 0.1;
% h.SpecularStrength = 0.1;
% h.SpecularExponent = 5;
% h.BackFaceLighting = 'unlit';
xlabel('mm');
ylabel('mm');
zlabel('mm');
```

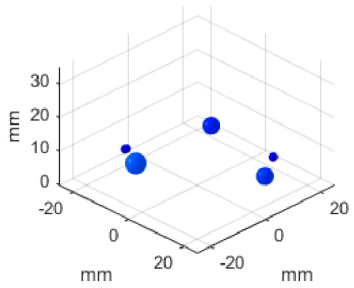

# Plot histogram

```
figure(4); clf;
hh = histogram(diameters,[0.5:1:round(max(diameters)/5)*5+5.5]);
nb = hh.Values;
vb = 1:length(nb);

nvol = 4*pi*(vb/2).^3/3;
%dff = floor((nvol/(4*V_init))*63)+1;
dff = floor((vb/d_max)*63)+1;
dff = dff';
col2 = zeros(length(nb),3);
for k=1:length(nb)
    if nb(k) == 0
    else
        a=dff(k);
        col2(k,:)=p(a,:);
    end
end

figure(4); clf;
b = bar(vb,nb);%,'grouped'
b.FaceColor = 'flat';
for k = 1:length(nb)
    b.CData(k,:) = col2(k,:);
end

xlabel('Aggregate Diameter (mm)');
ylabel('Frequency');
%title('Satellite Size Histogram');
xlim([0 30]);
ylim([0 20]);
xticks(0:5:30);
grid on;
set(gcf, 'Units', 'Inches', 'Position', [3, 3, 4*sc, 3*sc]);
```

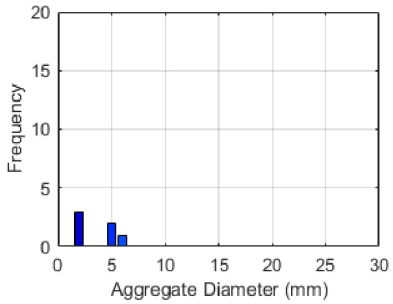

# Fluid volumes

```
V_wick = (V_init*4-sum(volume))/1000
V_wick_ratio = V_wick/(V_init*4/1000)

v1 = volume(find(diameters>5));
V_ratios = sort(v1/V_init,'descend')
```

```
V_wick =

   12.9758


V_wick_ratio =

    0.9833


V_ratios =

    0.0289
```

*Published with MATLAB® R2019a*

# Bibliography


[1] S. Oka *et al.*, "The effects of improper mixing and preferential wetting of active and excipient ingredients on content uniformity in high shear wet granulation," *Powder Technology*, vol. 278, pp. 266–277, 2015.

[2] F. J. Muzzio, T. Shinbrot, and B. J. Glasser, "Powder technology in the pharmaceutical industry: the need to catch up fast," *Powder Technology*, vol. 124, pp. 1–7, 2002.

[3] J. A. Hersey, "Powder Mixing: Theory and Practice in Pharmacy," *Powder Technology*, vol. 15, pp. 149–153, 1976.

[4] J. Bridgwater, "Fundamental Powder Mixing Mechanisms," *Powder Technology*, vol. 15, pp. 215–236, 1976.

[5] J. G. Osorio and F. J. Muzzio, "Evaluation of resonant acoustic mixing performance," *Powder Technology*, vol. 278, pp. 46–56, 2015.

[6] J. G. Osorio, E. Hernández, R. J. Romañach, and F. J. Muzzio, "Characterization of resonant acoustic mixing using near-infrared chemical imaging," *Powder Technology*, vol. 297, pp. 349–356, 2016.

[7] R. Tanaka, N. Takahashi, Y. Nakamura, Y. Hattori, K. Ashizawa, and M. Otsuka, "Verification of the mixing processes of the active pharmaceutical ingredient, excipient and lubricant in a pharmaceutical formulation using a resonant acoustic mixing technology," *RSC Adv.*, no. 6, 2016.

[8] J. G. Osorio, K. Sowrirajan, and F. J. Muzzio, "Effect of resonant acoustic mixing on pharmaceutical powder blends and tablets," *Advanced Powder Technology*, vol. 27, pp. 1141–1148, 2016.

[9] R. Y. Yee and E. C. Martin, "Effects of Surface Interactions and Mechanical Properties of Plastic Bonded Explosives on Explosive Sensitivity. Part 2: Model Finrmulation." Naval Weapons Center, 1985.

[10] F. J. Muzzio and A. W. Alexander, "Scale Up of Powder- Blending Operations." Pharmaceutical Technology, 2005.

[11] D. Barling, D. A. V. Morton, and K. Hapgood, "Pharmaceutical dry powder blending and scale-up: maintaining equivalent mixing conditions using a coloured tracer powder," *Powder Technology*, vol. 270, pp. 461–469, 2015.

[12] N. Harnby, "An engineering view of pharmaceutical powder mixing," *PSTT*, vol. 3, no. 9, pp. 303–309, 2000.

[13] M. D. Jones, J. G. F. Santo, B. Yakub, M. Dennison, H. Master, and G. Buckton, "The relationship between drug concentration, mixing time, blending order and ternary dry powder inhalation performance," *International Journal of Pharmaceutics*, vol. 391, pp. 137–147, 2010.

[14] A. Provatas, "Energetic Polymers and Plasticisers for Explosive Formulations - A Review of Recent Advances." DSTO, 2000.

[15] A. Provatas, "Formulation and Performance Studies of Polymer Bonded Explosives (PBX) Containing Energetic Binder Systems. Part I." Defence Science and Technology, 2003.

[16] S. R. Anderson, D. J. am Ende, J. S. Salan, and P. Samuels, “Preparation of an Energetic-Energetic Cocrystal using Resonant Acoustic Mixing,” *Propellants, Explosives, and Pyrotechnics*, vol. 35, pp. 1–5, 2010.
[17] L.-S. Lu and S.-S. Hsiau, “Mixing in vibrated granular beds with the effect of electrostatic force,” *Powder Technology*, vol. 160, pp. 170–179, 2005.
[18] J. Hilden, M. Sullivan, M. Polizzi, J. Wade, J. Greer, and M. Keeney, “Power consumption during oscillatory mixing of pharmaceutical powders,” *Powder Technology*, vol. 338, pp. 44–54, 2018.
[19] M. P. Makevnin, E. P. Aristova, and A. M. Gol’man, “Mixing Power in the Preparation of Powdered Composites,” *Khimicheskoe i Neftyanoe Mashinostroenie*, no. 5, pp. 6–7, 1989.
[20] J. F. Boyle, I. Manas-Zloczower, and D. L. Feke, “Hydrodynamic Analysis of the Mechanisms of Agglomerate Dispersion,” *Powder Technology*, vol. 153, pp. 127–133, 2005.
[21] A. Scurati, D. L. Feke, and I. Manas-Zloczower, “Analysis of the kinetics of agglomerate erosion in simple shear flows,” *Chemical Engineering Science*, vol. 60, no. 23, pp. 6564–6573, 2005.
[22] P. S. Raux, H. Cockenpot, M. Ramaioli, D. Quere, and C. Clanet, “Wicking in a Powder,” *Langmuir*, vol. 29, pp. 3636–3644, 2013.
[23] D. Brone, A. Alexander, and F. J. Muzzio, “Quantitative Characterization of Mixing of Dry Powders in V-Blenders,” *AIChE Journal*, vol. 44, no. 2, pp. 271–278, 1998.
[24] F. J. Muzzio, M. Llusa, C. L. Goodridge, N.-H. Duong, and E. Shen, “Evaluating the mixing performance of a ribbon blender,” *Powder Technology*, vol. 186, pp. 247–254, 2008.
[25] T. A. H. Simons, S. Bensmann, S. Zigan, H. J. Feise, H. Zetzener, and A. Kwade, “Characterization of granular mixing in a helical ribbon blade blender,” *Powder Technology*, vol. 293, pp. 15–25, 2016.
[26] P. Ratnayake, R. Chandratilleke, J. Bao, and Y. Shen, “A soft-sensor approach to mixing rate determination in powder mixers,” *Powder Technology*, vol. 336, pp. 493–505, 2018.
[27] A. Hassanpour, H. Tan, A. Bayly, P. Gopalkrishnan, B. Ng, and M. Ghadiri, “Analysis of particle motion in a paddle mixer using Discrete Element Method (DEM),” *Powder Technology*, vol. 206, pp. 189–194, 2011.
[28] I. M. Muslaev, S. Ya. Gzovskii, and I. N. Karasev, “Investigation of the Performance of Inclined-Paddle Radial Paddle Mixers Mixing Newtonian Fluids,” *Khimicheskoe i Neftyanoe Mashinostroenie*, no. 6, pp. 23–25, 1967.
[29] A. Valenberg and K. Wille, “Evaluation of resonance acoustic mixing technology using ultra high performance concrete,” *Construction and Building Materials*, vol. 164, pp. 716–730, 2018.
[30] L. L. Zhao, Y.-W. Li, X.-D. Yang, Y. Jiao, and Q.-F. Hou, “DEM study of size segregation of wet particles under vertical vibration,” *Advanced Powder Technology*, vol. 30, no. 7, pp. 1386–1399, 2019.
[31] E. L. Paul, V. A. Atiemo Obeng, and S. M. Kresta, *Handbook of industrial mixing science and practice*. Wiley-Interscience.

[32] B. Chaudhuri, A. Mehrotra, F. J. Muzzio, and M. S. Tomassone, “Cohesive effects in powder mixing in a tumbling blender,” *Powder Technology*, vol. 165, pp. 105–114, 2006.
[33] G. Ratkai, “Particle Flow and Mixing in Vertically Vibrated Beds,” *Powder Technology*, vol. 15, pp. 187–192, 1976.
[34] Y. Li and J. E. Sprittles, “Capillary breakup of a liquid bridge: identifying regimes and transitions,” *Journal of Fluid Mechanics*, vol. 797, pp. 29–59, Jun. 2016, doi: 10.1017/jfm.2016.276.
[35] S. P. Rwei and I. Manas-Zloczower, “Characterization of Agglomerate Dispersion by Erosion in Simple Shear Flows,” *Polymer Engineering and Science*, vol. 31, no. 8, pp. 558–562, Apr. 1991.
[36] D. F. Bagster and D. Tomi, “The Stresses Within A Sphere In Simple Flow Fields,” *Chemical Engineering Science*, vol. 29, pp. 1773–1783, 1974.
[37] S.-S. Hsiau and Y.-Y. Lin, “Segregation and convection of binary disks in a vertical shaker,” *Advanced Powder Technology*, vol. 11, no. 4, pp. 439–457, 2000.
[38] M. J. Metzger, B. Remy, and B. J. Glasser, “All the Brazil nuts are not on top: Vibration induced granular size segregation of binary, ternary and multi-sized mixtures,” *Powder Technology*, vol. 205, pp. 42–51, 2011.
[39] A. Jain, M. J. Metzger, and B. J. Glasser, “Effect of particle size distribution on segregation in vibrated systems,” *Powder Technology*, vol. 237, pp. 543–553, 2013.
[40] P.-G. de Gennes, F. Brochard-Wyart, and D. Quere, *Capillarity and Wetting Phenomena*. Springer, 2004.
[41] Z. Liu, Y. Wang, F. J. Muzzio, G. Callegari, and G. Drazer, “Capillary Drop Penetration Method to Characterize the Liquid Wetting of Powders,” *Langmuir*, vol. 33, pp. 56–65, 2017.
[42] capillary
[43] T. D. Blake and J. De Coninck, “The influence of solid liquid interactions on dynamic wetting,” *Advances in Colloid and Interface Science*, vol. 96, pp. 21–36, 2002.
[44] C. F. Lerk, A. J. M. Schoonen, and J. T. Fell, “Contact Angles and Wetting of Pharmaceutical Powders,” *Journal of Pharmaceutical Sciences*, vol. 65, no. 6, pp. 843–847, 1976.
[45] K. Muralidhar, “Equations Governing Flow and Transport in Porous Media,” in *Modeling Transport Phenomena in Porous Media with Applications*, Springer, pp. 15–63.
[46] B. M. Cummins, R. Chinthapatla, F. S. Ligler, and G. M. Walker, “Time-Dependent Model for Fluid Flow in Porous Materials with Multiple Pore Sizes,” *Analytical Chemistry*, vol. 89, pp. 4377–4381, 2017.
[47] A. Alghunaim, S. Kirdponpattara, and B. Zhang Newby, “Techniques for determining contact angle and wettability of powders,” *Powder Technology*, vol. 287, pp. 201–215, 2016.
[48] K. P. Hapgood, J. D. Litster, S. R. Biggs, and T. Howes, “Drop Penetration into Porous Powder Beds,” *Journal of Colloid and Interface Science*, vol. 253, pp. 353–366, 2002.

[49] Y. Yuan and T. R. Lee, “Contact Angle and Wetting Properties,” in *Surface Science Techniques*, Springer, pp. 3–34.
[50] T. Dang Vu and J. HUPKA, “CHARACTERIZATION OF POROUS MATERIALS BY CAPILLARY RISE METHOD,” *Physicochemical Problems of Mineral Processing*, vol. 39, pp. 47–65, 2005.
[51] S. Kirdponpattara, M. Phisalaphong, and B. Zhang Newby, “Applicability of Washburn capillary rise for determining contact angles of powders/porous materials,” *Journal of Colloid and Interface Science*, vol. 397, pp. 169–176, 2013.
[52] H. G. Bruil and J. J. van Aartsen, “The determination of contact angles of aqueous surfactant solutions on powders,” *Colloid and Polymer Science*, vol. 252, pp. 32–38, 1974.
[53] J. Xiao, H. A. Stone, and D. Attinger, “Source-like Solution for Radial Imbibition into a Homogeneous Semiinfinite Porous Medium,” *Langmuir*, vol. 28, pp. 4208–4212, 2012.
[54] H. Nadeem and T. J. Heindel, “Review of noninvasive methods to characterize granular mixing,” *Powder Technology*, vol. 332, pp. 331–350, 2018.
[55] M. Asachi, E. Nourafkan, and A. Hassanpour, “A review of current techniques for the evaluation of powder mixing,” *Advanced Powder Technology*, vol. 29, pp. 1525–1549, 2018.
[56] P. V. Danckwerts, “The definition and measurement of some characteristics of mixtures,” *Applied Scientific Research, Section A*, vol. 3, no. 4, pp. 279–296, 1952.
[57] D. I. Bigio and W. Stry, “Measures of mixing in laminar flow,” *Polymer Engineering and Science*, vol. 30, no. 3, pp. 153–161, 1990.
[58] M. Camesasca, M. Kaufman, and I. Manas-Zloczower, “Quantifying fluid mixing with the shannon entropy,” *Macromolecular Theory and Simulation*, vol. 15, pp. 595–607, 2006.
[59] J. G. Rosas and M. Blanco, “A criterion for assessing homogeneity distribution in hyperspectral images. Part 1: Homogeneity index bases and blending processes,” *Journal of Pharmaceutical and Biomedical Analysis*, vol. 70, pp. 680–690, 2012.
[60] L. Legoix, C. Gatumel, M. Milhé, and H. Berthiaux, “Characterizing powders in order to determine their flow behavior in a mixer: From small scale observations to macroscopic in-mixer rheology for powders of various flowabilities,” *Powder Technology*, vol. 322, pp. 314–331, 2017.
[61] Y. Zhang *et al.*, “Characterization of temporal and spatial distribution of bed density in vibrated gas-solid fluidized bed,” *Advanced Powder Technology*, 2018.
[62] M. A. Daniel, “Polyurethane Binder Systems for Polymer Bonded Explosives.” DSTO, 2006.
[63] A. Clarke, T. D. Blake, K. Carruthers, and A. Woodward, “Spreading and Imbibition of Liquid Droplets on Porous Surfaces,” *Langmuir*, vol. 18, pp. 2980–2984, 2002.
[64] L. Meng, P. Lu, and S. Li, “Packing properties of binary mixtures in disordered sphere systems,” *Particuology*, vol. 16, pp. 155–166, 2014.

[65] W. M. Visscher and M. Bolsterli, “Random Packing of Equal and Unequal Spheres in Two and Three Dimensions,” *Nature*, vol. 239, pp. 504–507, 1972.
[66] I. L. Davis and R. G. Carter, “Random particle packing by reduced dimension algorithms,” *Journal of Applied Physics*, vol. 67, pp. 1022–1029, 1990.
[67] T. Shinbrot and F. J. Muzzio, “Reverse Buoyancy in Shaken Granular Beds,” *Physical Review Letters*, vol. 81, no. 20, pp. 4365–4368, 1998.
[68] K. Liffman, K. Muniandy, M. Rhodes, D. Gutteridge, and G. Metcalfe, “A segregation mechanism in a vertically shaken bed,” *Granular Matter*, vol. 3, pp. 205–214, 2001.
[69] T. Akiyama and T. Naito, “Vibrated Beds Of Powders: A New Mathematical Formulation,” *Chemical Engineering Science*, vol. 42, no. 6, pp. 1305–1311, 1987.
[70] M. I. Khan and G. I. Tardos, “Stability of wet agglomerates in granular shear flows,” *Journal of Fluid Mechanics*, vol. 347, pp. 347–368, 1997.
[71] I. Figueroa, H. Li, and J. McCarthy, “Predicting the impact of adhesive forces on particle mixing and segregation,” *Powder Technology*, vol. 195, pp. 203–212, 2009.
[72] M. P. Dallimore and P. G. McCormick, “Distinct Element Modelling of Mechanical Alloying in a Planetary Ball Mill,” *Materials Science Forum*, vol. 235–238, pp. 5–14, 1997.
[73] H. Huang, M. P. Dallimore, J. Pan, and P. G. McCormick, “An investigation of the effect of powder on the impact characteristics between a ball and a plate using free falling experiments,” *Materials Science and Engineering: A*, vol. 241, pp. 38–47, 1998.
[74] C. M. Wensrich and A. Collard, “Resonant and non-linear behaviour in vibrationally fluidised beds,” *Powder Technology*, vol. 166, pp. 30–37, 2006.